

# **High-Energy Atmospheric Radiation: From Thunderstorm Ground Enhancements to Terrestrial Gamma-Ray Flashes**

**A. Chilingarian, L. Hovhannisyan, B. Sargsyan, and M. Zazyan**

**Yerevan Physics Institute, Alikhanyan Brothers 2, Yerevan, Armenia, AM0036**

## **Abstract**

It is widely recognized that the atmosphere shields the Earth from harmful radiation; however, understanding its active role in particle acceleration is essential for research in space weather and atmospheric physics. Thunderstorms generate strong atmospheric electric fields (AEFs) that extend over large areas within and around storm systems. The energy in AEFs mainly converts into radiation energy through relativistic runaway electron avalanches (RREAs, Gurevich et al., 1992), which appear as thunderstorm ground enhancements (TGEs, Chingarian et al., 2010, 2011) when detected on Earth's surface and as gamma glows when observed above intense tropical thunderstorms. Variations of these primary radiation sources include short gamma ray bursts recorded by orbiting gamma observatories at 500-700 km altitude, called terrestrial gamma ray flashes (TGFs, Fishman et al., 1994), and downward terrestrial gamma ray flashes (DTGFs, Ortberg et al., 2024), recorded in coincidence with lightning leader propagation.

This work presents a unified conceptual and observational framework that reinterprets these radiation bursts as manifestations of the same runaway processes happening at different atmospheric depths (Dual-stage model, DSM). We review recent results from satellite (ASIM), aircraft (ALOFT), balloon (HELEN), and ground-based (SEVAN and KANAZAWA) experiments to demonstrate the advantages of this integrated approach. This study addresses key contradictions in the field, introduces new classification criteria based on physics rather than detector location, and enhances our understanding of particle acceleration in thunderstorms.

## **Key Points:**

- **Unified physical mechanism:** TGEs, gamma glows, TGFs, and DTGFs are all outcomes of the RREA process occurring in different atmospheric regions.
- **Multi-platform data synthesis:** Includes results from ASIM (space), ALOFT (aircraft), Kanazawa (DTGF), and SEVAN (TGE).
- **A dual-stage, feed-forward coupling mechanism** in which a lower-dipole RREA supplies photons that seed electrons to upward RREA (DSM model).
- **A new model for DTGF origination:** field reorganization, not leader-gap acceleration.

- **Comparison of the measured electron TGE spectrum with theoretical expectations at different electric field strengths**

## 1. Introduction

Charge separation in thunderclouds, driven by updrafts of warm air and tension among hydrometeors, creates opposite dipoles within the cloud. C.T.R. Wilson, one of the first particle physicists and a pioneering researcher in atmospheric electricity, introduced a puzzling physical phenomenon known as “runaway” electrons at the start of the last century (see Chilingarian et al., 2025, and references therein). He proposed that free electrons are accelerated by the atmospheric electric field (AEF) into open space in the dipole between the main negatively charged region (MN) in the middle of the thundercloud and the main positive (MP) charge region at the top. However, Joachim Kuettner, conducting groundbreaking experiments at Zugspitze, discovered a more complex tripole charge structure within the charged layers of thunderclouds (Kuettner, 1950). According to the tripole model, the atmospheric electric field consists of upper and lower dipoles that accelerate free electrons both toward open space and the Earth's surface. Not everyone immediately understood the significance of Kuettner's discovery. In 1963, Richard Feynman wrote: “The top of the thunderstorm is positively charged and the bottom negative, except for a small local area of positive charge at the bottom of the cloud, which caused much concern for everyone. No one seems to know why he is there or how important he is. If it weren't for him, everything would be much easier” (Feynman et al., 1963). However, further investigations of cloud charge structure (Williams, 1989) confirm the tripole structure of cloud charge and the role of “graupel” hydrometeors in forming the transient LPCR. According to modern theories, LPCR is essential for charge separation within the cloud and the initiation of lightning (Nag & Rakov, 2009; Chilingarian et al., 2017a). Without it, lightning would most likely strike toward the upper positive charge. Thus, without this “useless” local area of positive charge, our planet might be quiet, dark, and lifeless.

Free electrons from Extensive air showers (EASs, Auger et al., 1939) are abundant in the troposphere. The altitude of the electron maximum density, known as the Regener–Pfozter maximum, depends on the geomagnetic cutoff rigidity ( $R_c$ ), and the phase and intensity of the solar cycle. Recent measurements, confirmed by PARMA4 calculations (Sato, 2016), show that the peak flux of charged particles occurs in equatorial regions ( $R_c = 10\text{--}15$  GV) at an altitude of 16–17 km (Fig. 4 of Ambrozova et al., 2023). Electric fields generated by intense thunderstorms transfer energy to free electrons, accelerate them, and, under certain conditions, produce electron-photon avalanches. In 1992, Gurevich, Milikh, and Roussel-Dupré established conditions for the extensive multiplication of electrons from each energetic seed electron injected into the region of a strong electric field (Gurevich et al., 1992). This process is now called the Relativistic Runaway Electron Avalanche (RREA; Babich et al., 2001; Alexeenko et al., 2002). A numerical approach for solving the relativistic Boltzmann equation for runaway electron beams (Symbalisty et al., 1998) helps estimate the threshold (critical) electric field (Babich et al., 2001; Dwyer et al., 2003) required to initiate RREA. At standard temperature and pressure in dry air at sea level,  $E_{th} \approx 2.80 \cdot n$  kV/cm (density-scaled threshold), where air density  $n$  is relative to the International Standard Atmosphere (ISA) sea-level value (see the recent update of the critical energy  $E_{th} \approx 2.67 \cdot n$  kV/cm in Dwyer and Rassoul, 2024). This threshold field is slightly higher than the breakeven field, which corresponds to the electron energy at which minimum ionization occurs. If electrons traveled exactly along electric field lines, this would define the threshold for runaway electron propagation and avalanche formation. However, the paths of electrons deviate due to Coulomb scattering with atomic nuclei and Møller scattering with atomic electrons, leading to deviations from the ideal case. Moreover, secondary electrons produced by Møller scattering are not

generated along the field line; therefore, electric fields 10-20% stronger are needed for electrons to run away and initiate an avalanche. In Figure 1, we illustrate the radioactive terrestrial atmosphere, which is bombarded by billions of cosmic rays (CR) entering from space and originating in the atmosphere and the Earth's crust. The atmospheric radiation sources are shown on the left side of the diagram. The lower dipole comprises the main negative layer and an induced mirror charge on the Earth's surface. Another dipole forms between the main negative layer and LPCR, which is often associated with falling graupel (snow pellets coated with a layer of ice, Kuettner, 1950). Electrons accelerated by the two lower dipoles generate electron-gamma ray avalanches, which are detected as thunderstorm ground enhancements (TGEs; Chilingarian et al., 2010, 2011). Due to the proximity of the electron accelerators in thunderclouds to the surface, TGEs contain millions of gamma rays, electrons, positrons, and neutrons. Particle detectors beneath electron accelerators at high-altitude sites in Armenia, Eastern Europe, Germany, and other locations have recorded hundreds of TGEs, confirming extensive particle fluxes over thousands of square kilometers and durations ranging from seconds to tens of minutes (Chum et al., 2020; Chilingarian et al., 2024a). Data from Aragats have convincingly validated the RREA/TGE model through direct measurements of electron and gamma-ray spectra, which have also detected atmospheric neutrons and positrons (Chilingarian et al., 2012, 2024b). Importantly, these measurements show good agreement with predicted energy spectra (Dwyer, 2003) and highlight the role of seed electrons from EASs.

The dipole between the LPCR and its mirror in the Earth accelerates positrons and positive muons while decelerating electrons and negative muons (Chilingarian et al., 2024a; 2024b). The LPCR is temporary and vanishes with the fall of graupel, causing rapid changes in the cloud's charge structure. This, in turn, quickly alters the AEF and the acceleration and deceleration modes of charged particles.

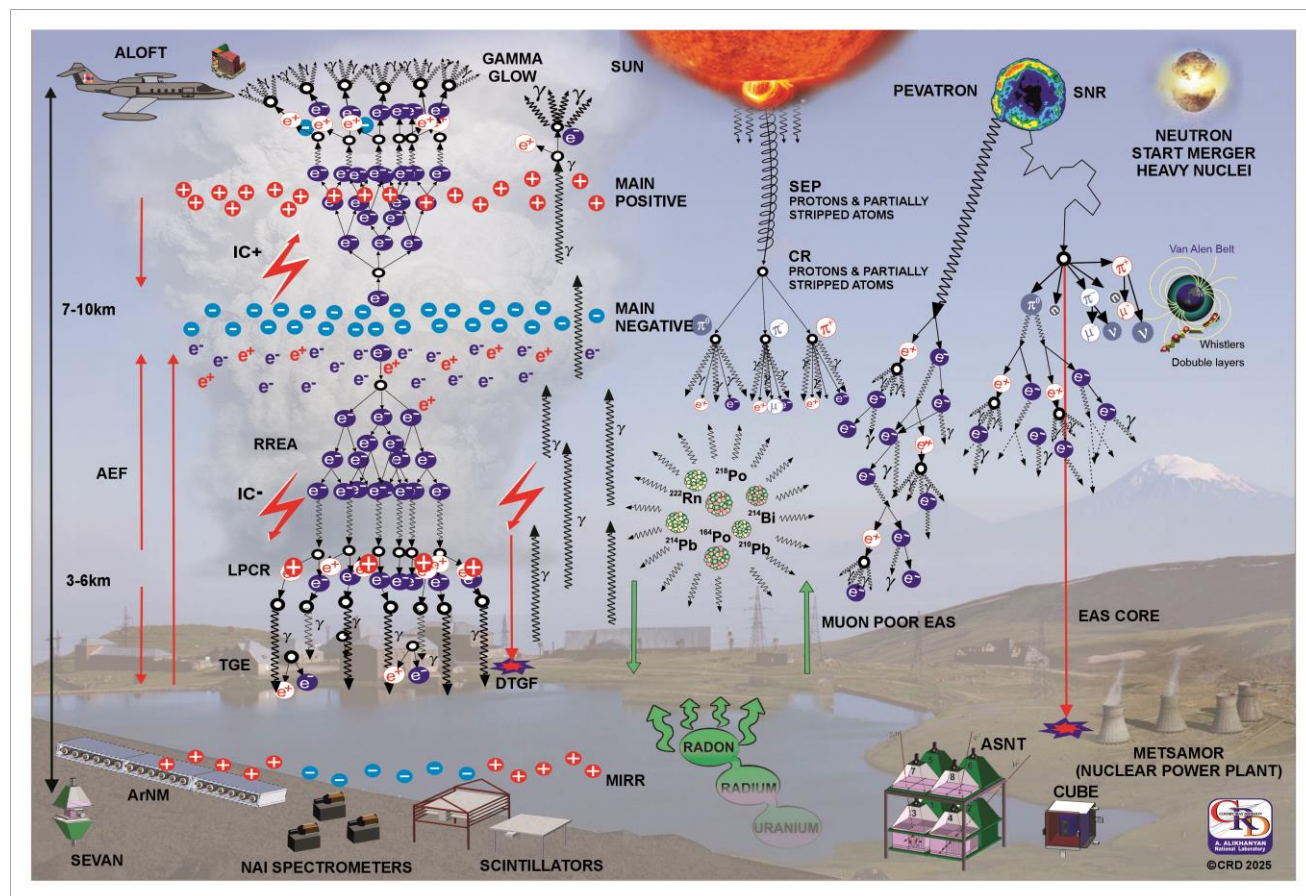


**Figure 1. The fluxes of secondary particles from space and atmospheric accelerators, as well as gamma radiation from  $^{222}\text{Rn}$  progeny. Additionally, the diagram shows the sources of primary cosmic rays. In the background, the Aragats cosmic ray station, situated at an elevation of 3200 meters, is equipped with various particle detectors and spectrometers.**

The upper dipole consists of the main negative and main positive charge layers (see Fig. 1). Electrons accelerated within this dipole generate avalanches in the upper atmosphere, leading to gamma-ray glows detected by airborne experiments flying above thunderstorms (Kelly et al., 2015; Ostgaard et al., 2019; Marisaldi et al., 2024; Helmerich et al., 2024). Additionally, some gamma rays reach orbiting gamma observatories 400-700 km away from the source, triggering microsecond bursts of particles known as terrestrial gamma flashes (TGFs, Fishman et al., 1994; Mailyan et al., 2015). The dipoles in the lower atmosphere rely on a relatively stable downward flux of free electrons from EASs as seeds to generate RREAs, which are observed on Earth's surface as TGEs. The difficulty in providing seeds to trigger RREA in the upper dipole has persisted for the past 30 years. It is not possible to reverse the downward electrons to initiate RREA in the upper dipole. Several proposed sources of seeds moving upward face significant difficulties (see review Chilingarian, 2024).

To overcome these challenges, we propose a two-stage, vertically coupled RREA mechanism that links a lower, downward-accelerating region—where strong RREAs generate bremsstrahlung—to an upward-accelerating region that continuously transforms gamma seed flux into gamma-ray glows observed in the upper atmosphere. We will demonstrate that a fraction of gamma rays from the lower dipole, redirected by Compton scattering, combined with conversion near the start of the upper dipole and kilometer-scale upper-dipole fields, can sufficiently account for the magnitude, duration, and altitude of upward glows without requiring a single, unrealistically bright gamma-ray source, usually introduced to explain TGF fluxes. (Mailyan et al., 2015)

The right side of Fig. 1 illustrates the EASs formed high in the atmosphere by galactic gamma rays, protons, and fully stripped nuclei interacting with atmospheric atoms. High-energy particles are produced during violent explosions and mergers within the galaxy and beyond. The diagram shows a supernova remnant and a neutron star merger. When cosmic-ray-induced extensive air showers develop in the atmosphere, their lateral spread can reach several hundred meters to several kilometers, depending on the primary energy and altitude. The cores of EAS contain the highest-energy secondary particles, creating very short, compact bursts indicated by the red circle. Muon-poor events detected at altitudes above 4000 meters suggest Pevatrons- stellar sources that accelerate protons up to  $10^{15}$  eV. The illustration also features a nuclear power plant, a potential source of radioactive contamination, and the Van Allen belt, which can emit MeV electrons toward Earth.

## **Corsika simulations of RREAs reaching Aragats stations and comparisons with the electron flux recovered from observed TGEs**

The direct evidence of the RREA process in a thunderous atmosphere is the detection of RREA electron flux. The first measurement of electron flux during thunderstorms at Aragats on September 19, 2009 (Chilingarian et al., 2017b), marked the beginning of High-Energy Physics in the Atmosphere (HEPA) research, which continues to this day. The historical background of surface RREA observations and the reasons for their delayed recognition over many decades are detailed in Chilingarian et al. (2025). In this section, we describe TGE research details, comparing RREA energy spectra modeled with the CORSIKA code and TGE observations. We used the CORSIKA code (Heck et al., 1998), version 7400, which includes electric field effects in particle transport (Buitink et al., 2010).

The growth of RREA increases the cloud's electrical conductivity. Studies in New Mexico (Marshall et al., 1995; Stolzenburg et al., 2007) have shown that lightning flashes occur after the AEF exceeds the RREA initiation threshold. RREA simulation codes do not include a lightning initiation mechanism. Therefore, one can artificially increase the electric field strength beyond realistic levels to generate billions of avalanche particles; however, this approach lacks physical justification. As a result, we do not test electric fields stronger than 2.2 kV/cm at altitudes of 3-6 km.

The RREA simulation used vertical seed electrons and a uniform electric field that exceeded the  $E_{th}$  by 10-30% at an altitude of 5,400 meters. However, applying a uniform electric field produces different excess percentages over  $E_{th}$  at various altitudes, depending on air density. The seed electron energy spectrum was based on the EXPACS WEB calculator (Sato, 2016), following a power law with an index of -1.25 for energies from 1 to 300 MeV. The ambient secondary cosmic ray population at 5-6 km altitude contributed approximately 42,000 seed electrons per square meter per second with energies above 7 MeV, as estimated with EXPACS. During large TGE events, the typical distance to the cloud base is estimated to be 25–100 m (see Fig. 17 in Chilingarian et al., 2020). To study electron flux decay, particle propagation continues through dense air for an additional 100 m before detection. The simulations included 1,000 to 10,000 events for electric field strengths ranging from 1.8 to 2.2 kV/cm, as shown in Fig. 2. Electron and gamma-ray propagation was tracked until their energies dropped to 0.05 MeV. The number of RREA particles was recorded every 200 m in the AEF and every 25 m after leaving the AEF.

In Figure 2, we show the development of the RRE avalanches at different atmospheric depths and for various physically justified strengths of the intracloud electric field. The curves are recalculated using a single seed electron for easier comparison with experimentally measured intensities. For the lower electric field strengths (1.8 and 1.9 kV/cm), the RREA process attenuates before reaching the observation level at 3200 m, at a depth of 2100 m (see the red and yellow curves in Fig. 2).

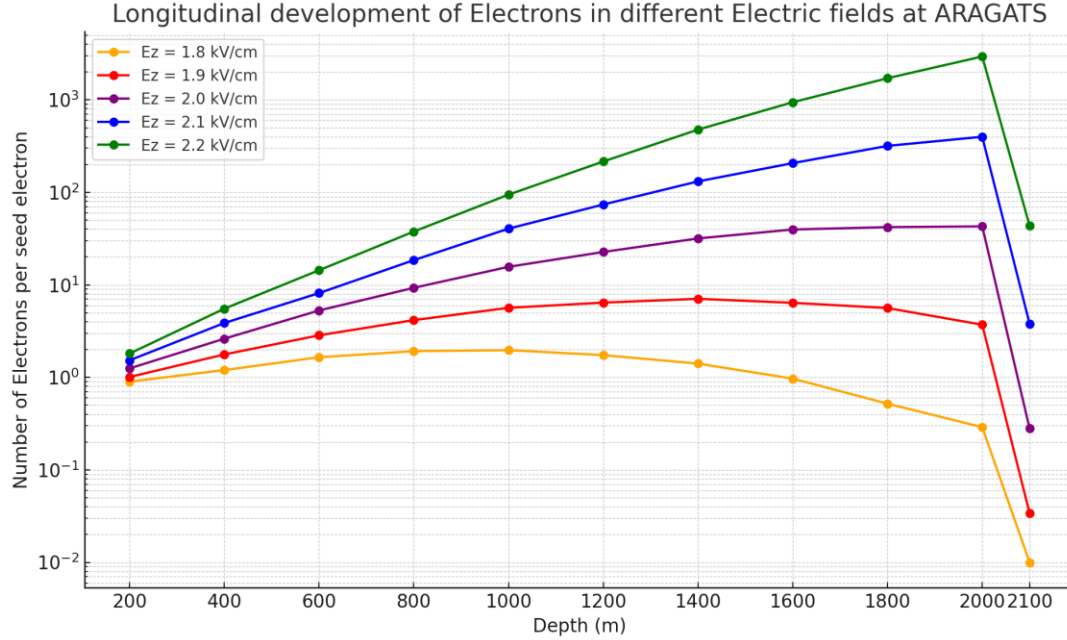


**Figure 2. Development of the RRE avalanche in the lower dipole. The avalanche began at 5400 m a.s.l. (0 meters depth), which is 2100 meters above the Aragats station. The number of avalanche particles is calculated every 200 meters. After exiting the electric field, the propagation of avalanche particles is tracked for an additional 100 meters before reaching the station, which is located at 2100 m depth.**

We continuously supported TGE measurements on Aragats with simulations of the RREA process in AEFs. Previously, we compared these simulations with the TGE recorded on June 14, 2020 (Chilingarian et al., 2021). In this paper, we analyze the TGE that occurred on October 2, 2024, at 00:43. Particle detectors on Aragats registered a significant increase in particle flux count rate, as shown in Fig. 3. This was the first and only TGE of 2024 with a large electron content. The enhancement of low-energy gamma-ray and electron flux detected by the stacked 3-cm-thick, 1-m<sup>2</sup>-area STAND3 plastic scintillator (see Chilingarian and Hovsepian, 2023, coincidence 1000, red curve) reached 225% ( $125\sigma$ ). The “1100” coincidence of the same detector (green curve) selected electrons with energies above 20 MeV. The 20-cm-thick, 0.25-m<sup>2</sup>-area spectrometric SEVAN light scintillator (Chilingarian et al., 2024) detected electrons with energies above 10 MeV (blue). Gamma-ray peaks are typically much larger (black and red curves), reflecting the rapid attenuation of electrons upon leaving AEF.

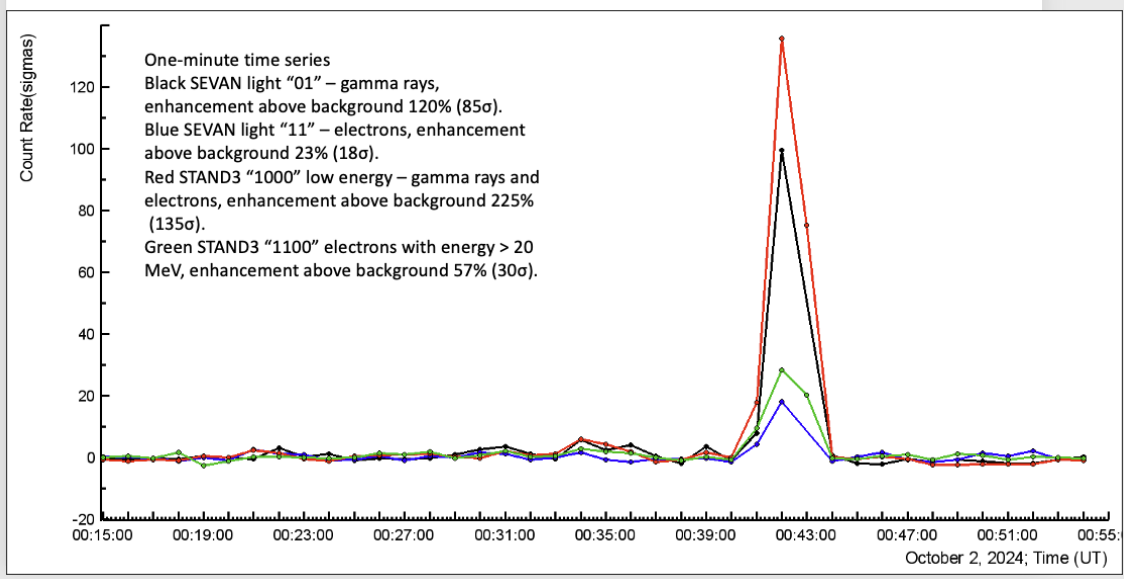


**Figure 3. One-minute time series of count rates for SEVAN light (black and blue) and STAND3 detectors (red and green).**

More details on TGE are shown in Fig. 4. A one-second time series of the count rate from a 1 cm thick, 1 m<sup>2</sup> outdoor scintillator on the roof of the GAMMA experiment's calorimeter shows nearly a tenfold increase (850%, 120 $\sigma$ ). The black curve illustrates the NSEF, which is deeply negative during TGE. A broad peak started at 00:41:40, reached a maximum at 00:42:35, and then declined at 00:43:15 before immediately rising again until a cloud-to-ground (-CG) lightning flash abruptly stopped TGE at 00:43:36. The RREA electron flux in the cloud was intense enough to create an ionization channel in the lower atmosphere, providing a path for the lightning leader (see Chilingarian et al., 2017a).

In the inset of Fig. 4, we show the distance to the cloud base, estimated by the spread (difference between outside temperature and dew point), using the well-known meteorological approximation equation (Spread, 2025):

$$H(m) \approx (\text{Air temperature at surface } \{^{\circ}\text{C}\} - \text{dew point temperature } \{^{\circ}\text{C}\}) \times 122 \quad (1)$$

The distance is minimal (60 m) at the flux maximum. This explains a 3.5-fold increase in gamma-ray flux compared to the electron flux, as measured by the SEVAN light spectrometer (5744 vs. 1660). Electrons were attenuated over 60 m before reaching the detector.

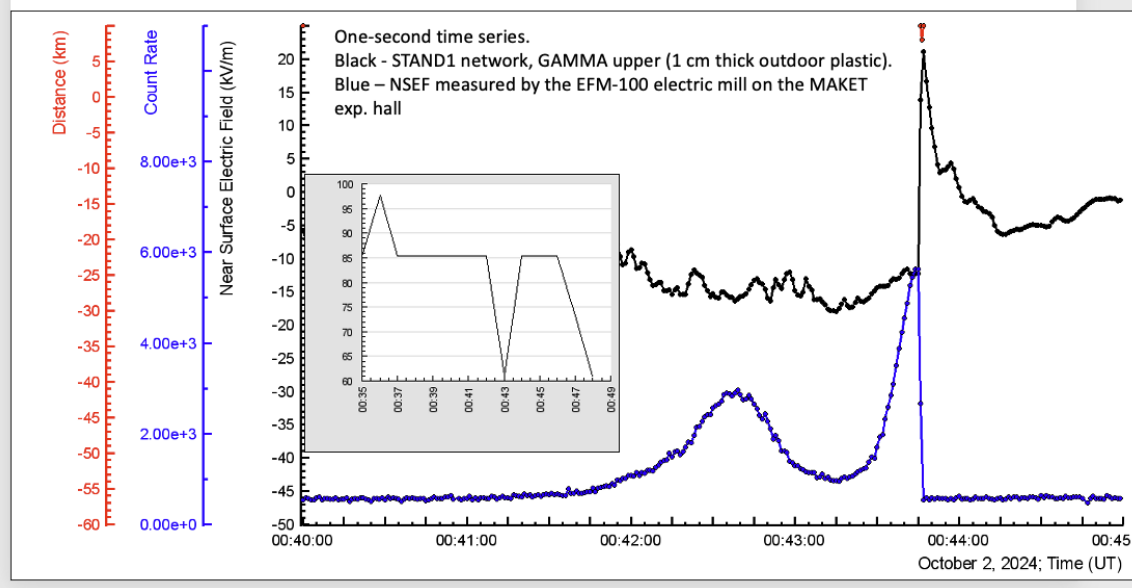


**Figure 4. One-second time series of the STAND1 detector (blue) and measurements of NSEF (black curve). In the inset – distance to the cloud base.**

In Figure 5, we present the differential energy spectrum of electrons measured above the roof of the SKL experimental hall, where the SEVAN light spectrometer is positioned. The detector response was unfolded using a GEANT4-based response matrix, following the inverse-problem method outlined in Chilingarian et al. (2022). The spectrum is well described by a simple exponential function in energy and aligns with the form given by Eq. 17 in Dwyer & Babich

(2011). The maximum electron energy reaches approximately 34 MeV.

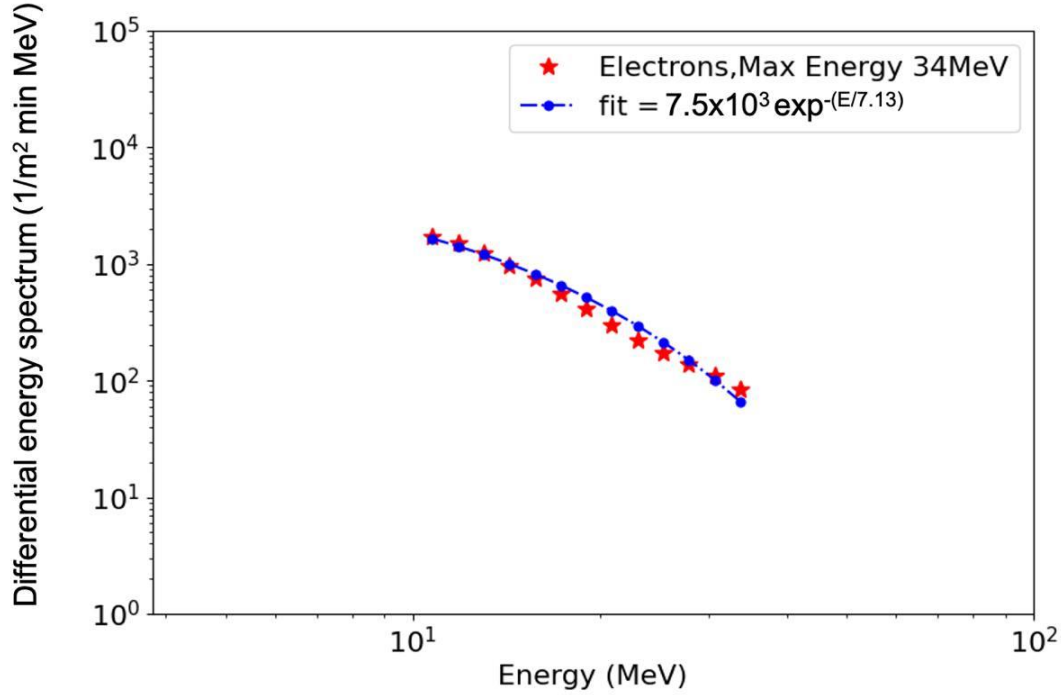


**Figure 5.** *Differential energy spectrum of TGE electrons above the roof of the SKL experimental hall (SEVAN light spectrometer).*

We integrated the recovered differential spectrum above 10 MeV to obtain the integral electron flux (counts min<sup>-1</sup> m<sup>-2</sup>), which is directly comparable to CORSIKA simulations. The per-seed multiplication factors used in the comparison are taken from CORSIKA and represent the mean number of electrons with energies >10 MeV that reach the detector level for each injected seed electron at 5.4 km a.s.l. Simulations were run for several intracloud field strengths  $E_z$  and accelerating-field extents  $L$ , with avalanches tracked down to the Aragats station (3.2 km). The measured and simulated integral fluxes (count rates) are compared in Table 1. We include the TGE of 14 June 2020 (a moderate event) and 2 October 2024 (a strong event).

**Table 1. Comparison of simulated and measured electron fluxes for 2 TGE events occurred on 14 June 2020 and 2 October 2024**

Case	Field $E_z$ (kV/cm)	AEF extent $L$ (km)	Termination Above Detector (km)	Measured $\Phi(>10$ MeV) (counts min <sup>-1</sup> m <sup>-2</sup> )	Simulated $\Phi(>10$ MeV) (counts min <sup>-1</sup> m <sup>-2</sup> )

2020 small TGEs	1.8–1.9	$\approx 1.0\text{--}1.5$ ( $\leq 1.2$ for 1.8)	0.10–0.20	$\sim 2\text{--}5 \times 10^3$	$\sim 2\text{--}4 \times 10^3$
2024 strong TGE (best)	$\approx 2.0$	$\approx 2.0$	0.06	$1.31 \times 10^4$	$1.35 \times 10^4$
2024 strong TGE (alt.)	$\approx 2.1$	$\approx 1.2\text{--}1.4$	0.06	$1.31 \times 10^4$	$1.28 \times 10^4$

The comparisons of simulated data shown in Fig.1 with the experimentally measured energy spectrum in 2020 (Fig. 4 of Chilingarian et al., 2021a) and 2024 (Fig. 5) yield the following conclusions:

- 2020 TGE. Measured and simulated integral fluxes agree within a factor of  $\sim 1.2\text{--}1.5$ , which is comfortably inside expected variability from atmospheric conditions and instrumental uncertainty. The accelerating field was (1.8–1.9 kV/cm) and elongation (1.0–1.5 km), with the lower boundary 100 m above the detectors. For such not-very-large TGEs, the AEF range is under  $\sim 1.5$  km and the potential drop is under  $\sim 250$  MV.
- 2024 strong TGE. Simulations with  $E_z = 2.0\text{--}2.1$  kV/cm and  $L = 2.0$  km reproduce the measured integral flux with high accuracy. The potential drop can exceed  $\sim 400$  MV.
- Higher fields (e.g., 2.2 kV/cm) overshoot the intensity and are inconsistent with the data.

Therefore, both the 2020 and 2024 TGEs support RREA originating in the lower dipole, starting at 5.4 km a.s.l., and extending to the lower AEF boundary, located tens to hundreds of meters above the detectors. The shorter termination height inferred for 2024 naturally explains its much higher flux. The shorter termination heights in 2024 compared to 2020 account for the significantly larger fluxes observed in 2024. This agreement supports the interpretation that TGEs at Aragats are produced by RREAs initiated in thunderclouds above the station, with their strength and vertical extent governing the resulting ground-level flux.

Modelling AEF and the development of RREA within it were based on many simplifications. The strengths and spatial extent of the electric field, cloud height, and seed electron energy spectrum are assumed in the simulation. However, they are in overall agreement with in situ measurements, but can significantly deviate from the conditions of the particular thunderstorm that gave rise to the detected TGE event. Therefore, the energy spectra obtained in simulation trials provide only an overall estimate of the particle yield on the surface. We also made some assumptions about the termination of the AEF, relating it to the spread. Although this method is widely used in meteorology, we cannot one-to-one identify the AEF termination with cloud base height. Therefore, we develop an empirical method based on the maximum energies of the measured electron and gamma-ray spectra (see Chilingarian et al., 2022).

Using the Mendeley dataset (Chilingarian and Hovsepyan, 2021), we recovered the electron differential energy spectra by analyzing 16 TGE events and estimated the heights of the field

termination above the ground. The distance at which the strong accelerating field is terminated (free passage distance, FPD) is determined using CORSIKA simulations by an empirical equation tuned on available electron spectra (Spread, 2025):

$$\text{FPD (meters)} = (C1 * E_{\text{max}}^{\gamma} - E_{\text{max}}^e) / C2 \quad (2),$$

We identify the highest energies of electrons and gamma rays from recovered energy spectra. Coefficients C1 and C2 are 1.2-1.4 and 0.2, respectively. TGE simulations indicate that the maximum energy of electrons leaving the electric field is 20-40% higher than that of gamma rays. Therefore, we estimate the maximum energy of electrons exiting the field as  $C1 * E_{\text{max}}$ . We performed multiple simulations of electron-gamma ray avalanches to verify the accuracy of equation (2) and check for potential methodological errors. We record particle energies and solve the inverse problem to recover RREA characteristics from measured TGE data. We use CORSIKA simulations with different electric field strengths and termination heights to achieve this. Subsequently, we follow all experimental procedures on the obtained samples to estimate the maximum energies of electrons and gamma rays. Then, we calculate the FPL parameter using equation (2) and compare it to the "true" value from the simulation. Based on this comparison, we estimate the method's mean square deviation (MSD) as 50 meters, as shown in Table 12 of Chilingarian et al. (2022, supplementary materials). Using the maximum energies of gamma rays (28 MeV) and electrons (30 MeV), we estimate the FPD on October 2, 2024, to be  $50 \pm 50$  meters. This estimate is consistent within one standard deviation with the value derived from "meteorological" data, which is 60 m, according to the spread (Eq. 1).

Another piece of evidence for the strong AEF on October 2, 2024, is the significant depletion of the muon flux, which supports the idea of an extended electric field above the detector. The same electric field that accelerates electrons also reduces positive muons, and because of a charge ratio of 1.2–1.3, the muon counts in the scintillator show substantial depletion; see Fig. 6. It also highlights that TGE can be used to estimate the maximum electric field in the thundercloud (see Fig. 4 and Table 2 in Chilingarian et al., 2022).

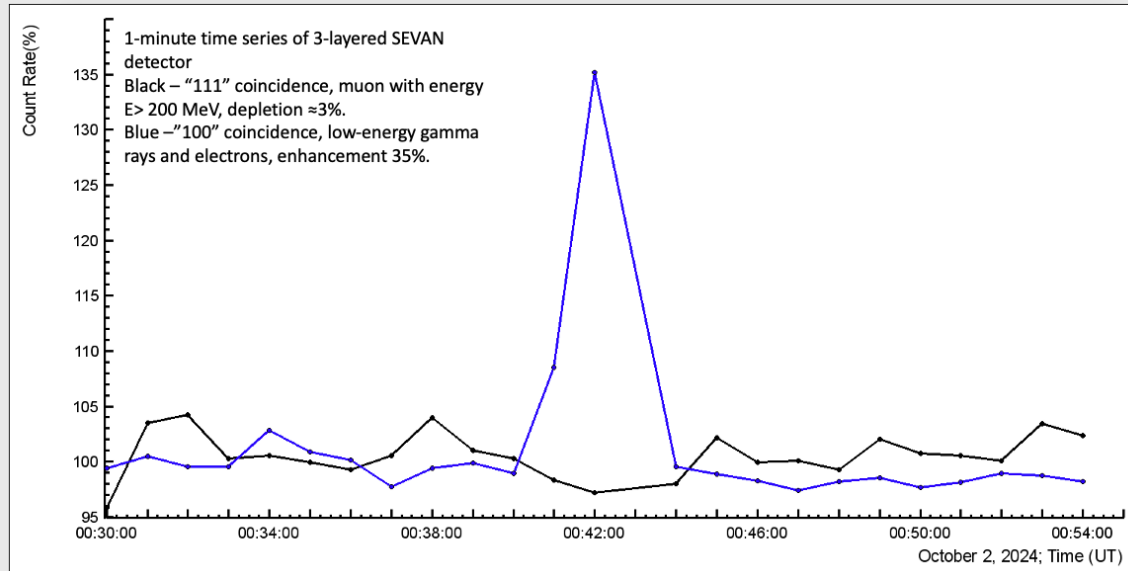


**Figure 6. One-minute time series of the SEVAN-Aragats detector, showing black low-energy gamma rays and electrons, and blue high-energy muons.**

Based on key measurements of the TGE electron and gamma-ray energy spectra, along with observations of neutron and muon flux modulation effects on Aragats and worldwide (Chilingarian et al., 2025), we conclude that the RREA model with EAS seeds fully explains electron-photon avalanches in the lower atmosphere. A comprehensive model of enhanced particle fluxes in the upper atmosphere and space has yet to be developed. The biggest challenge is identifying the source of seed electrons. EAS electrons and positrons move downward, while generating a population of upward-moving electrons presents a significant challenge.

### **Enhanced particle fluxes above thunderstorms: the seed electrons problem**

Historically, the earliest evidence of high-energy radiation in the upper atmosphere comes from decades of balloon and aircraft observations of intense gamma-ray bursts at altitudes of 8-15 km (see discussion and references in Ostgaard et al., 2019). These measurements, often interpreted as manifestations of the MOS process (Chilingarian, Mailyan, and Vanyan, 2012), assume that the AEF did not exceed the runaway threshold at altitudes of 15-20 km. However, the source of seed electrons remains unclear.

In the lower dipole, the ambient downward-moving cosmic-ray electrons align with the downward-directed electric field and easily initiate RREA. In the upper dipole, however, the field points upward, opposite to the momentum of the ambient cosmic-ray electrons; CORSIKA simulations show that such particles do not supply significant numbers of upward  $>1$  MeV seeds. Therefore, the seed mechanism for upper-dipole RREA is fundamentally different from that at lower altitudes.

There is extensive evidence, ranging from early balloon and NASA’s F-106 jet flights (Parks et al., 1981; McCarthy et al., 1985) to recent aircraft-based observations (Kelley et al., 2015; Kochkin et al., 2017; Ostgaard et al., 2019), that lightning abruptly halts particle fluxes in the upper atmosphere. This suggests a relationship between the two phenomena and warrants further investigation into RREA seeds in lightning initiation. It has been proposed that a small-scale electric field at the lightning leader tip can be strong enough to initiate RREA and produce abundant seed electrons, resulting in an extremely bright source with up to  $10^{20}$  fluence (cold runaway model, Celestin & Pasko, 2011). In 2012, the relation between lightning and TGF was thought to be firmly established (Dwyer et al., 2012): “TGFs are produced in what are structurally normal IC flashes during the period when the initial negative polarity leader travels upward from the main negative charge layer to the upper positive layer. This occurs during the first 5–10 ms of the lightning flash, but distinctly after the flash initiation. TGFs occur during the ascent of this upward leader before it reaches and expands into the upper positive charge layer. Inferred altitudes of the leader tip at the time of TGF generation have ranged from approximately 11 to 15 km.

In 2024, this relationship seemed to be smeared (Dwyer, Rassoul, 2024): “Currently, TGFs are thought to be produced inside thunderclouds during the initial stage of upward positive intra-cloud (IC) lightning. However, the relationship between lightning and TGF production is unclear, and it is also not well understood why some lightning produces TGFs while others do not. In addition to spacecraft observations, X-rays and gamma rays are emitted by thunderclouds, as observed using both in situ and ground-based techniques. These emissions often form gamma-ray “glows” lasting seconds to minutes (thunderstorm ground enhancements when observed from the ground). Many of these observations exhibit energy spectra similar to TGFs, which extend into the multi-MeV range, indicating a similar source mechanism. In 2025, it was firmly declared that “thunderstorms may generate intense gamma-ray emissions without lightning” and TGFs can be created by “thunderstorm electrification alone, without the presence of lightning...” (Dwyer, 2025).

Thus, recent measurements and reanalysis of TGF catalogs do not support the “lightning” scenario of TGF origination (see review Chilingarian, 2024, and references therein). TGFs, measured alongside lightning flash detections by ASIM instruments, prove that there are no observed events where the optical pulse onset precedes the onset of the TGF. The median determined delay between onsets is 190  $\mu$ s (Skeie et al., 2022). In the multi-pulse patterns of TGFs registered by ASIM (Fig. 6.6 of Fuglestad, 2023), we can see that the first TGF detected at 18:02:25 on July 5, 2021, smoothly finished, and no optical images of the atmospheric discharges were observed. The second TGF, which occurred 2 ms later, was terminated by a lightning flash, as seen in both the abrupt termination of particle flux and the optical signal. Zhang et al. (2021) demonstrated that gamma rays are produced several milliseconds before a narrow bipolar event, which often marks lightning initiation. Analysis of four TGF catalogs from different instruments revealed that a significant proportion of TGFs lead to increased lightning activity detected in radio waves (spherics) between 150-750 ms after TGFs occur (Lindanger et

al., 2022). Furthermore, in a recent paper (Gourbin and Celestin, 2024), the maximum achievable number of electrons from “cold runaway” was limited to  $10^{17}$ .

The Airborne Lightning Observatory (ALOFT, Ostgaard et al., 2024) conducted cutting-edge experiments in 2023, measuring multiple gamma glows from tropical thunderstorms. ALOFT payload consists of five spectrometers, 30 photometers, three electric-field sensors, two radars, and two passive radiometers. Particle fluxes were monitored during flight, and gamma-ray-glowing clouds were identified in real-time to facilitate return and continuation of measurements. ALOFT detected more than five hundred gamma-ray glows during nine of the ten flights, showing that thunderclouds can emit gamma rays for hours and over huge regions (see Fig. 1 of Marisaldi et al., 2024). Glows were detected repeatedly following consecutive passages (aircraft revisited flaring thunderclouds after notification of mission physicists) over the same thundercloud system, covering  $\approx 10^4$  km<sup>2</sup>.

Correlated measurements of ALOFT and ASIM reveal several gamma-ray fluxes observed by ALOFT but not by ASIM during the ISS overpass. The authors (Björge-Engeland et al., 2024) conclude that the overwhelming gamma glow population directed to space from tropical thunderclouds is too weak to be observed from space. The source photon brightness of gamma glows is several orders of magnitude lower than what is usually attributed to TGF observed by orbiting gamma observatories. Thus, TGFs comprise only a small percentage of gamma glows copiously observed above tropical storms, as numerous TGEs are observed on the Earth’s surface. In our opinion, gamma glows and TGFs may represent different observational manifestations of the same underlying high-field radiation process; only a very small fraction of the upward-directed “glow gamma rays” are favorably oriented to be detected by satellites at altitudes of hundreds of kilometers.

Thus, the ALOFT experiment provided groundbreaking insights, demonstrating that gamma glows and TGFs were immediately followed by Narrow Bipolar Events (NBEs), initiating significant lightning activity. These findings challenge prior hypotheses that lightning leaders supply the seed electrons for TGFs. Recent measurements from ALOFT and long-term nanosecond-scale monitoring of atmospheric discharges and particle fluxes at Aragats strongly support an alternative hypothesis: relativistic runaway electron avalanches precede and initiate the lightning leader (Chilingarian et al., 2015, 2017b). The combination of gamma-ray imaging and lightning interferometry proposed by the ALOFT continuation can directly test and validate this transformative hypothesis.

The ALOFT findings, which demonstrate the role of thunderclouds as huge natural particle accelerators, confirm ground-based observations obtained by continuously monitoring particle fluxes and electric fields within large areas around Aragats Mountain (Chilingarian et al., 2022; Chilingarian et al., 2024c). Thus, the joint study of TGEs and gamma glows will enhance fundamental knowledge of high-energy physics in the atmosphere (HEPA), clarifying key issues

related to particle acceleration and lightning initiation while bridging the gap between processes in the lower and upper atmosphere (Dwyer et al., 2012).

Observations of ALOFT (Marisaldi et al., 2024; Ostgaard et al., 2024), conducted 1-2 kilometers above gamma-ray sources, yield groundbreaking findings that demonstrate the existence of extensive and prolonged gamma-ray emission regions, contradicting earlier theoretical models used for 30 years to explain TGFs. These newly characterized phenomena, such as Flickering Gamma-ray Flashes (FGFs) and Glow Bursts (GBs), challenge models featuring intense, distributed gamma-ray sources and open a fresh frontier in the RREA/gamma glow models, making them similar to the RREA/TGE model.

In the next section, we will show how the hybrid Compton-redirected gamma rays' mechanism (the dual-stage model, DSM)—where strong RREAs in the lower dipole produce upward Compton-redirected gamma rays—naturally accounts for both the flux level and the vertical size of gamma glows observed by ALOFT.

#### **4. Dual-stage model: RREA mechanism for upward gamma-ray glows**

While it is generally understood that the physical mechanism responsible for atmospheric radiation is RREA, the source of seed electrons varies. Historically, TGFs are modeled with highly intense local gamma sources, with fluence reaching up to  $10^{19}$ . In contrast, TGEs are modeled with seeds from EAS electrons, providing a well-measured, stable, altitude-dependent flux over large volumes of thundercloud systems. Persistent, upward-directed gamma-ray glows observed by ALOFT and balloon experiments—covering areas greater than or equal to 10,000 km<sup>2</sup> and lasting from tens of minutes to hours—cannot be explained by short, localized very bright discharge scenarios (e.g., classic TGF models). Therefore, we propose a dual-stage, vertically coupled mechanism in which a lower-dipole RREA supplies photons that seed an upper-cloud RREA, thus naturally producing a sustained gamma flux that extends into space across large areas ( $\sim 10^4$  km<sup>2</sup>), spans multiple kilometers vertically, and persists for several tens of minutes.

The issue of seed formation for the upward-moving avalanche has been essential since the TGF discovery in 1994 (Fishman et al., 1994), and it has become even more pressing after the detection of intense gamma-ray flybys with the ALOFT experiment (Marisaldi et al., 2024). However, unlike the lower dipole, the physics of electron acceleration in the upper dipole remains not fully understood. In this paper, we will analyze in detail the physical processes that seed relativistic runaway electron avalanches (RREAs) in the upper dipole, leading to particle bursts in the upper atmosphere and space. To prevent misunderstandings about the codes used and the interpretation of simulation results, we will add simplified theoretical considerations of particle interactions in the upper atmosphere to the simulation results.

In the CORSIKA code, the atmospheric electric field (AEF,  $E_z$ ) negative sign indicates electron acceleration toward open space, while the positive sign indicates electrons accelerating toward Earth's surface (physical notation). The notation for atmospheric electricity used in geophysics uses reverse notation: positive AEF indicates accelerated electrons toward open space, and negative AEF indicates electrons moving toward Earth's surface (atmospheric electric field notation). In this section, we will use the physical notation accepted by CORSIKA authors.

The downward ambient cosmic ray (CR) flux provides electron seeds for the RREA developing in the lower dipole. For RREA to develop in the upper dipole, seeds must move upward, opposite to the CR flux. CR electrons in the upper dipole will be stopped by AEF; however, positrons will be accelerated and multiplied if AEF exceeds the runaway threshold. Additionally, gamma rays can travel freely through the AEF of either polarity. We will consider all channels that supply upward-moving electrons for RREA development in the upper dipole. MeV positrons can trigger RREA avalanches, and gamma rays from these avalanches can produce electron-positron pairs ( $\gamma \rightarrow e^- + e^+$ ), resulting in some upward electrons. CR gamma rays can also generate electrons through pair production. Furthermore, bremsstrahlung and Compton-scattered electrons can be directed upward. We will examine all sources of upward electrons that serve as seed electrons entering the bottom of the upper dipole.

For calculation and simulation purposes, we should choose realistic parameters based on the RREA process in the atmosphere, justified by both theoretical considerations and extensive experience with RREA detection in the lower dipole.

## 5. RREA development calculation and simulation

We adopted the tripole structure of the AEF (Kuettnner, 1950). The tripole was positioned within the 5.3-7.3 km range (lower dipole) and the 7.3-9.3 km range (upper dipole). A uniform electric field was introduced within these dipoles. Since the AEF length is quite long, for theoretical considerations, we divided the 2 km into 10 slabs of 200 m each and calculated the seed yield for each. Consideration of RREA multiplication will be based on the notion of e-folding length and the multiplication rate. The e-folding length  $\lambda$  is the characteristic distance over which the number of runaway electrons increases by a factor of  $e$ .

$$N(z) = N_0 e^{(z/\lambda)}.$$

It quantifies the avalanche growth rate and depends heavily on:  $E_z$ , the AEF strength;  $E_{th}$ , the runaway threshold field;  $\rho$ , the local air density.

Dwyer (2003, 2012) and Babich (2007) derived a convenient parameterization:

$$\lambda(E, \rho) = \frac{73 \text{ kV/cm}}{E - E_{th}(\rho)} \times \frac{\rho_0}{\rho},$$

where:  $E_{th}(\rho)$  or  $E_{th}(h)$  is the threshold (critical) field for runaway,  $\rho_0 = 1.225 \text{ kg/m}^3$  is air density at sea level, and  $\rho$  is air density at altitude.

The total multiplication along AEF length  $L$  is approximately:

$$M = \exp(L/\lambda).$$

The dependence of threshold  $E_{th}(h)$  on altitude was determined by extrapolating CORSIKA simulations for the following heights: 2.0 km to 2.3 km, 2.7 km to 2.1 km, 3.3 km to 1.9 km, and 4.5 km to 1.7 kmV/cm. These values were obtained from multiple simulations with stepwise AEF growth; the threshold was set at the AEF where particle exponential growth was detected (Chilingarian et al., 2025). In Fig. 7, we show this dependence extrapolated to 10 km (green). The blue curve shows a 40% enhanced threshold AEF at which RREA will be mature, and lightning flashes still will not quench AEF. We perform calculations for various values of  $E_z > E_{th}$ , but aim to stay within physically justifiable limits. Recall that after a 30-40% increase above the threshold, lightning flashes typically quench the potential difference and terminate RREA (Stolzenburg et al., 2007). Previously, we estimated the maximum electric field (potential drop) on the mountain tops of Lomnicky Stit (Chilingarian et al., 2021b) and Aragats (Chilingarian et al., 2021c), with results in good agreement with direct measurements. The e-folding length corresponding to a 40% enhanced AEF is shown by the black curve. The inset displays the numerical values of the dependences at three different heights.

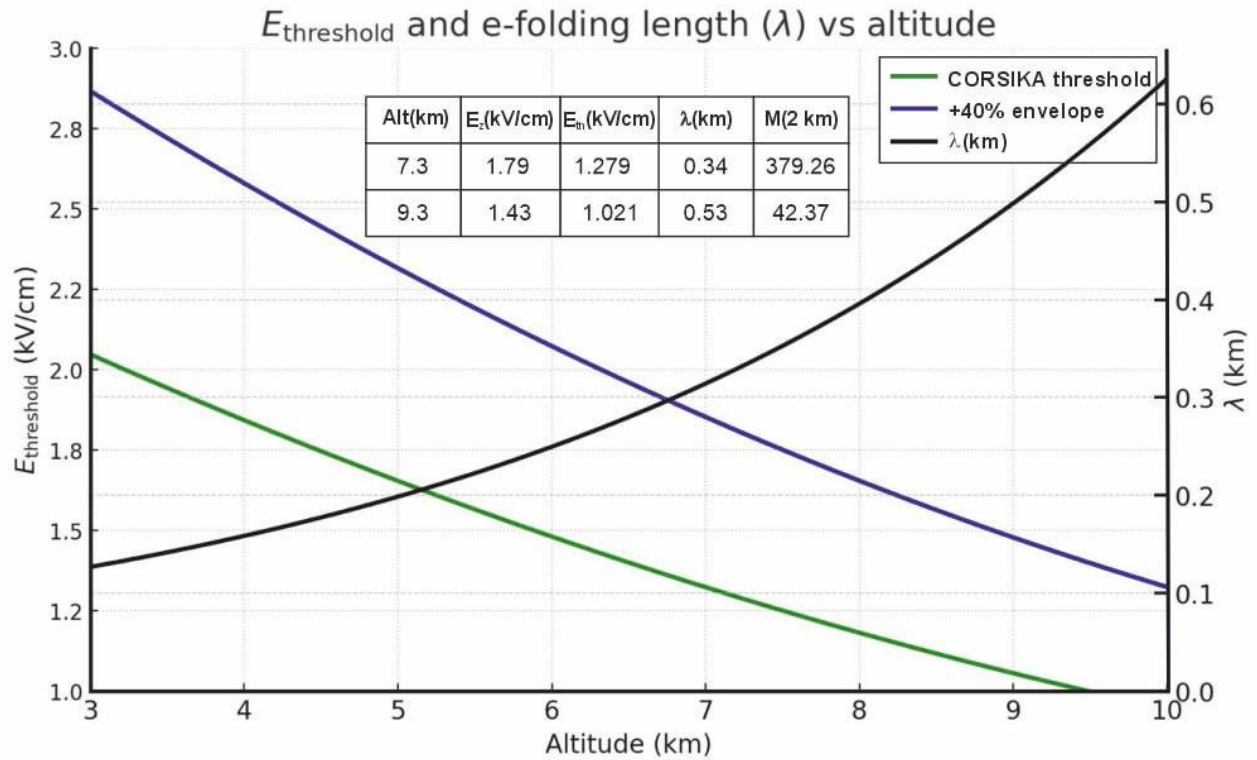


**Figure 7. Altitude dependence of the threshold AEF and e-folding length. In the inset, we show a 40% enlarged  $E_z$  used in calculations and the avalanche growth factor  $M$  in 2 km of field.**

In Figure 8, we show the unlimited growth of RREA particles with increasing AEF. Clearly, this growth is not physically justified, so we set a limit on it, indicated by the red line.

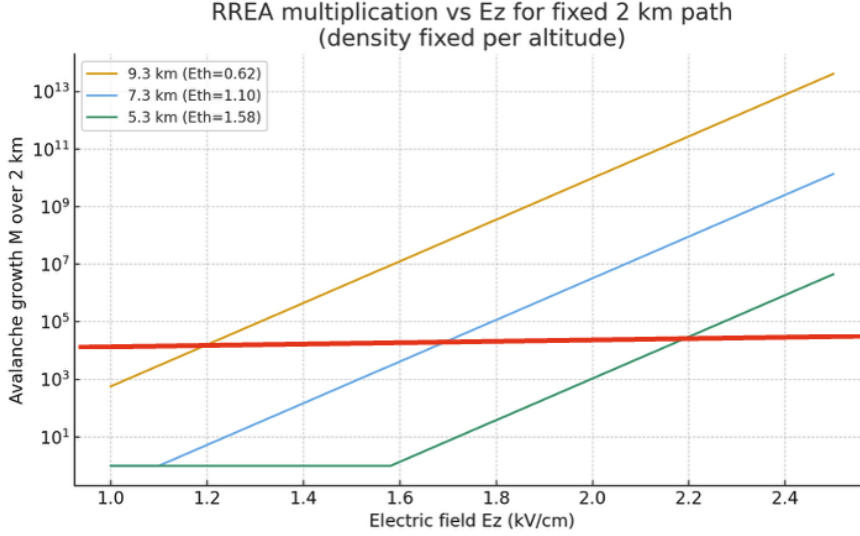


**Figure 8. RREA multiplication factor (avalanche growth) depends on  $E_z$  for different altitudes. The red line shows the limit set for multiplication rates to be  $10^4$ .**

The limit for avalanche multiplication was set at  $10^4$  based on our experience with TGE detection in the lower dipole (Chum et al., 2020; Chilingarian et al., 2024a). Within this limit, we use different AEF values, including those exceeding a 40% increase over the threshold AEF, to better understand possible extreme scenarios of upward-directed seeds. We simulate interactions of gamma-ray and positron beams with air and analyze the resulting upward lepton fluxes. A total of 1,000,000 positrons and gamma rays are injected vertically downward from 9.3 km altitude into a 200 m air slab ending at 9.1 km and 7.1 km. Their initial energy distributions follow power laws  $dN/dE \propto E^{-1.125}$  and  $E^{-2}$  between 1 and 100 MeV. The downward electric fields, with magnitudes of 2.1 and 2.4 kV/cm, accelerate positrons and decelerate electrons. All gamma rays emitted, scattered upward, and reaching 9.3 and 7.3 km altitude are recorded and analyzed. The mechanisms governing the production and propagation of upward-moving gamma rays and secondary particles in atmospheric electric fields are considered and discussed.

To track both downward and upward particle fluxes, we use CORSIKA 8, built on the well-established foundation of CORSIKA 7. It extends capabilities beyond air showers to include particle cascades in arbitrary media, such as by introducing AEFs (Engel et al., 2019).

In Figure 9, we present the energy release histograms for all four simulations with extreme electric fields. Red lines indicate the fits for low and high-energy domains separately. The annihilation line at 511 keV appears in all four frames with varying intensities. Other features in

the spectra include bumps around 200 keV in frame c and near 1 MeV in frame d.

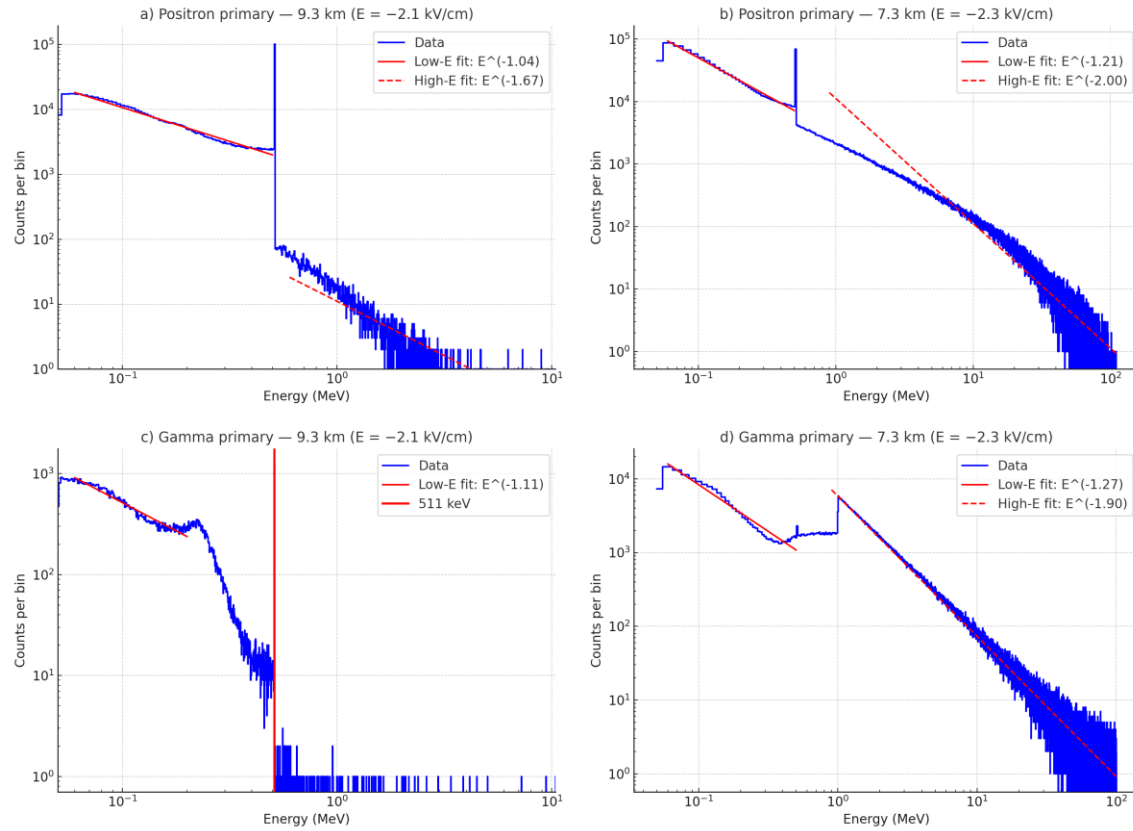


**Figure 9. Energy release histograms of backscattered gamma ray yield from incident gamma-ray and positron ambient fluxes at 7.3 and 9.3 km traversing 200 m of AEF.**

At energies below about 0.5 MeV, the observed gamma-ray spectrum is shaped by the combined effects of Compton scattering and bremsstrahlung. In this sub-MeV range, photons from bremsstrahlung and positron annihilation undergo multiple Compton scatterings in air. Each scattering reduces the photon energy and alters its direction, producing a nearly isotropic diffuse flux directed upward. This process, known as Comptonization, transforms an initially hard bremsstrahlung spectrum into a quasi-flat continuum with an effective slope of about  $-0.9$ , consistent with the expected behavior of partially degraded bremsstrahlung in a low-density target (Pozdnyakov, Sobol & Sunyaev, 1983). The bump around 200 keV in frame c originates from Compton backscattering and photon-photon interactions occurring when the downward  $\gamma$ -beam produces upward-moving photons with energies near 200–230 keV — the most probable energy of scattered.

At 7.3 km, the higher density shortens the mean free paths of electrons and photons, increasing the probability that bremsstrahlung photons are degraded to the sub-MeV range before escaping. This explains the observed enhancement of the sub-MeV flux at lower altitude. Pair production also affects this energy range through a feedback loop. High-energy photons (above 1.02 MeV) produce electron-positron pairs, which then emit secondary bremsstrahlung photons mainly in

the MeV range. Many of these photons are subsequently Compton-scattered down to hundreds of keV, contributing to the sub-MeV continuum. Therefore, the low-energy region reflects the combined effects of primary bremsstrahlung degradation, reprocessing of annihilation photons, and downscattering of secondary photons from pair-production feedback.

A weak 511 keV feature and its Compton shoulder (notably in frame b) result from annihilation at rest, where roughly half the photons escape upward. In-flight annihilation contributes to the mid-range continuum (0.4–1 MeV), blending with soft bremsstrahlung.

The downward-moving positrons emit bremsstrahlung photons reaching up to tens of MeV, creating the MeV continuum. Bremsstrahlung is the primary emission mechanism for MeV photons. Downward electric fields accelerate electrons upward from avalanche populations. As these electrons collide with atmospheric nuclei, they emit a broad, continuous spectrum extending up to tens of MeV. The bremsstrahlung emission rate depends on both the electrons' energy and the local air density. At 7.3 km, where collisions are more frequent, emissions are more efficient compared to 9.3 km. The simulated MeV tails in the spectra (frames a, b, d) indicate this increased production of high-energy photons.

High-energy gamma rays ( $>1.02$  MeV) can interact with atmospheric nuclei to create electron-positron pairs. This process provides a feedback loop, where newly born positrons are accelerated downward, emitting secondary bremsstrahlung, while electrons are accelerated upward, contributing to the high-energy component of the upgoing flux.

*The newly born electrons, accelerated upward by the electric field, emit additional bremsstrahlung photons in the upward direction. This secondary process forms the high-energy tail and triggers a relativistic runaway electron avalanche (RREA).*

The sub-MeV continuum originates from Compton-degraded photons, while the MeV tail is replenished by bremsstrahlung from electrons accelerated in RREA and by pair-production feedback. The intersection of these components forms a local hump near 1 MeV (frame d), clearly visible in the positron-beam case due to the higher supply of radiating electrons. Analysis of the raw spectra confirms that upward photon fluxes are higher at 7.3 km for positron primaries in the sub-MeV region, and that both primary types exhibit stronger MeV-range regeneration at 7.3 km because of enhanced electron acceleration and pair feedback. The  $\sim 1$  MeV hump thus represents a robust spectral signature of the balance between Compton degradation and bremsstrahlung/pair regeneration.

At 9.3 km, the runaway threshold is approximately 1 kV/cm, and the simulated field of 2.1 kV/cm is roughly twice this value. At 7.3 km, the field (2.3 kV/cm) is about 75% above the local threshold, so both layers satisfy the RREA condition ( $E > E_{th}$ ). Thus, upward electron avalanching enhances the high-energy tail of the spectra in both cases. However, despite the smaller  $E/E_{th}$  ratio at 7.3 km, the resulting high-energy gamma-ray flux is much larger (see frames b and d). This occurs because the air density and grammage within 200 m below 7.3 km are more than twice those at 9.3 km, increasing the bremsstrahlung yield and pair-production probability. Consequently, the denser layer produces a significantly stronger MeV photon output even under a slightly less supercritical field.

Positron-initiated showers involve significant bremsstrahlung losses during deceleration in the electric field, thereby enhancing secondary electron production and increasing upward gamma-ray yield. Positron primaries generate more MeV photons and a harder spectrum. Since air density is higher at 7.3 km than at 9.3 km, the strong electric field boosts the RREA yield and the contribution of upward-electron bremsstrahlung in the MeV range. Thus, under AEF exceeding

threshold values, RREA contributes to the formation of intense upward gamma-ray flux observed during balloon and aircraft flights.

The different scenarios for obtaining upward flux of leptons are detailed in Table 2, where we show lepton upward fluxes above 50 keV and 1 MeV for various AEFs, dipole elongations, and ambient CR incident fluxes.

**Table 2. Summary of upgoing lepton probabilities for the single downgoing ambient lepton.**

CORSIKA simulated probabilities (calculated from 1 million trials)	Ne+ (>1MeV)	Ne+ (>50KeV)	Ngamma (>1MeV)	Ngamma (>50KeV)	Ne- (>1MeV)	Ne- (>50KeV)
Upper_dipole_9,3 - 9,1 km observation level 9,35 km. -1.5kV/cm incident particle gamma.	0,000001	0,000001	0,00004	0,094	0	0,000011
Upper_dipole_9,3 - 9,1 km. observation level 9,35 km. -2.1kV/cm incident particle gamma.	0	0	0,00005	0,094	0	0,00005
Upper_dipole_9,3 - 9,1 km. observation level 9,35 km. -1.5KV/cm incident particle positron.	0,000004	0,000004	0,00020	0,0691	0,000069	0,00016
Upper_dipole_9,3 - 9,1 km. observation .evel 9,35 km. -2.1kV/cm incident particle positron.	0,000005	0,000005	0,00021	0,0697	0,000095	0,00018
Upper_dipole_9,3 - 7,3 km. observation level 9,35. -2.1kVcm incident particle positron.	0,000007	0,000007	0,00121	0,375	0,000184	0,00082
Lower_dipole_7,3 - 5,3 km. observation level 7,35. +1.9kV/cm incident particle electron.	1,06	1,1	0,45	1,65	0,000222	0,000247

The data in the first 5 rows of 21 estimate the likelihood that downward ambient cosmic ray populations are reversed and return to the upper dipole top to sustain the upward gamma-ray flux observed by particle detectors on balloons and aircraft. We estimate these probabilities (per single-incident lepton) using the upper 200 m of the dipole and the full 2 km length.

Additionally, we compare realistic 1.5 kV/cm AEF and a value double the threshold, 2.1 kV/cm AEF, introduced in the first 200 m of the dipole, to examine the influence of electric field strength on the probability of upward seeds. In the last row, we show the electron flux upward at 7.3 km altitude from the ambient electron flux that initiates RREA in the lower dipole in the 5.3-7.3 km gap. This allows us to compare possible mechanisms for generating upward gamma ray flux. We will also estimate the potential for an infinite feedback model (Dwyer, 2003, 2025; Babich, 2007) aimed at explaining intense upward gamma ray flux.

As shown in Table 2, the chance that downgoing ambient cosmic-rays produce an upward-moving MeV electron capable of initiating RREA in the upper dipole is only about  $10^{-6}$  to  $10^{-5}$  per particle. Even with twice-threshold fields (2.1 kV/cm), upward MeV electrons are nearly absent. These values are too small to sustain upward RREA. Only a very small number of sub-MeV particles (<100 keV) appear due to Compton scattering of gamma rays, but these low-energy electrons cannot trigger RREA.

Table 2 shows that ambient positron flux produces more upward-going photons than gamma primaries. This occurs because energetic positrons in the downward electric field emit bremsstrahlung photons at wide angles and are scattered upward, acting as natural seeds for producing upward-moving electrons. The same process happens with electrons moving downward in the opposite field of the lower dipole, where their bremsstrahlung also creates upward-directed photons. In contrast, gamma primaries produce fewer upward photons because Compton scattering and pair production distribute energy more evenly, resulting in only a small fraction of radiation escaping upward. Hence, we will consider only positron-originated RREA in the upper dipole.

For 200 m, the gamma yield at 1.5 and 2.1 kV/cm is about the same. In the first 200 m, the positron RREA isn't developed. Over the entire 2 km, the RREA is fully established, and the upward gamma-ray flux is roughly 5 times higher. At a lower dipole, the production of upgoing  $\gamma$ -rays is about 4 times greater, as the downgoing electron beam interacts with the atmosphere's denser, thicker layer. Although AEF at the 9.3 km region is well above the runaway threshold (field strength = 2.1 kV/cm, twice the  $E_{th}$ ), the air density there is roughly 40% lower than at 7.3 km, with over 200 m of grammage being twice as much at the lower altitude. Two main effects occur: a reduced collision rate—fewer air molecules mean bremsstrahlung and pair-production cross sections per unit path length decrease, leading to fewer upward photons—and longer mean free paths—photons produced there are less likely to scatter or convert within 200 m, with most escaping the volume without secondary interactions. Therefore, although all electrons and positrons could theoretically run away, they produce far fewer bremsstrahlung photons than in the denser layer at 7.3 km, and they exit the electric field region without generating gamma rays. As a result, at high altitudes, the feedback strength diminishes.

## 6. The scheme of the feedback mechanism and estimation of infinite feedback possibilities.

In Dwyer's infinite feedback model, the mutual coupling between upward-moving electron avalanches and downward-moving positron avalanches creates a closed loop: each generation of gamma rays produces pairs that supply new seeds of opposite charge traveling in the direction that sustains the field-driven cascade. In theory, this process could lead to exponential growth of relativistic particles if the feedback coefficient ( $\Gamma$ ) equals or exceeds one. However, under realistic atmospheric densities and electric-field strengths, most gamma rays are absorbed within 2 km of the air gap, and the likelihood of both pair production and favorable emission direction is very low ( $>0.1\%$ ). As a result, the feedback coefficient remains several orders of magnitude below 1, preventing the development of a self-sustaining or "infinite" feedback loop. Within  $L=2$  km of AEF, the air density varies significantly. Therefore, we divide 2 km AEF into 10 slabs, each of  $\Delta h = 200$  m, and estimate particle propagation step by step. The mass thickness of a single slab is approximately  $\rho \times \Delta h$ , where  $\rho$  is air density; at 7–9 km. The backward-going gamma-ray flux that reaches to 9.3 km from  $i$ -th slab can be represented as the following track:

$$N_{\gamma}^{\uparrow}(i \rightarrow 9.3 \text{ km, from } e^+ \text{ and } e^- \text{ RREA}) = \{M_{e^+}^{\downarrow}(i, E_z, \gamma > 1.022 \text{ MeV}) \times P_{\text{pair}}(h_i) \times f_{\uparrow}(e^-) \times T_i(9.3 \text{ km})\} + \{M_{e^-}^{\uparrow}(i, E_z, \gamma > 1.022 \text{ MeV}) \times P_{\text{pair}}(h_i) \times f_{\uparrow}(e^-) \times T_i(9.3 \text{ km})\} \quad (1)$$

Infinite feedback (recursive term):

$$\text{New cycle multiplication} = N_{\gamma}^{\uparrow}(i \rightarrow 9.3 \text{ km, from } e^+ \text{ and } e^- \text{ RREA}) \times \{M_{e^+}^{\downarrow}(i, \gamma, E_z) \times P_{\text{pair}}(h_i) \times f_{\uparrow}(e^-) \times T_i(9.3 \text{ km})\} \quad (2)$$

The downward-moving positron avalanche produces gamma rays in each slab, and gamma-ray energy must exceed 1.022 MeV to enable pair production. The electron energy should be above 1 MeV to allow RREA to ascend in the opposite direction of the positron avalanche (with a very small probability, but not zero). Downward-propagating positron RREA and upward-propagating electron RREA generate gamma rays that can produce pairs in each slab. Since this occurs in every slab, the contributions from all slabs must be summed. The multiplication in RREAs was derived from the e-folding length, assuming a 40% surplus of AEF relative to the e-folding length, as shown in Fig. 7.

$$M_{e^+}^{\downarrow}(i, \gamma, E_z) = e^{\frac{L_{\text{rem}}(i)}{\lambda}} \quad (3)$$

$L_{\text{rem}}(i)$  is the remaining distance to 9.3 km for which pair production and RREA multiplication are evaluated,  $\lambda$  - avalanche e-folding length in the upper dipole at fixed atmospheric electric field. Correspondingly:

The multiplication in the up-running electron avalanche from slab  $i$ , including  $\gamma$  survival to 9.3 km.

$$\boxed{M_{e^-}^\uparrow(i, \gamma, E_\gamma) = e^{-\frac{L_{\text{rem}}(i)}{\lambda}}} \quad (4)$$

The probability that at least one pair production event occurs within  $\Delta X$  is therefore:

$$P_{\text{pair}(i)} = 1 - e^{-\Delta X / \Lambda_{\text{pair}(i)}} \quad (5)$$

where  $\Delta X$  is the mass thickness of a single slab ( $\approx \rho \times \Delta h$ ) mass of air in  $\text{g cm}^2$  and  $\Lambda_{\text{pair}}$  is the pair-production mean free path for photons with  $E_\gamma > 1 \text{ MeV}$ , expressed in  $\text{g cm}^{-2}$ .

In the thin-slab limit, the pair probability follows from the Beer–Lambert equation (Mayerhöfer et al., 2020); the spectrum-weighted pair coefficient  $(\mu_{\text{pair}}/\rho)_{\text{eff}}$  is:

$$P_{\text{pair}}(i) = 1 - e^{-(\mu/\rho)_{\text{pair}} \rho_i \Delta z}. \quad (6)$$

Where  $\mu$  is the linear attenuation coefficient for 1 MeV  $\gamma$  rays,  $\approx 6.3 \times 10^{-5} \text{ cm}^{-1}$ . At  $E_\gamma \sim 1 - 3 \text{ MeV}$ , the *effective* mass total attenuation coefficient for MeV photons, dominated by pair production  $(\mu/\rho)_{\text{pair}}$  is roughly  $\sim 10^{-4} - 10^{-3} \text{ cm}^2/\text{g}$ . We adopt  $(\mu_{\text{pair}}/\rho)_{\text{eff}} = 1.07 \times 10^{-4} \text{ cm}^2 \text{ g}^{-1}$ .

Exponential attenuation law:

$$\boxed{T_i(9.3) = e^{-\frac{L_{\text{rem}}(i)}{\Lambda(E_\gamma)}}} \quad (7)$$

where

- $L_{\text{rem}}(i)$ — **vertical grammage** ( $\text{g cm}^{-2}$ ) of air between the emission altitude and 9.3 km;
- $\Lambda(E_\gamma)$ — **effective attenuation length** for photons of energy  $E_\gamma$ , typically 60–120  $\text{g cm}^{-2}$  in the 0.1–10 MeV range;
- $\rho(h)$  — altitude-dependent air density, which determines  $X(h) = \int \rho \, dz$ .

The Compton scattering cross-section and energy–angle redistribution are described by the Klein–Nishina formula (Klein & Nishina, 1929), which strongly favors forward scattering at MeV energies. For 2 km of air, the attenuation factor is  $T(9.3) \approx 0.37$ , meaning that only about one-third of photons above 1 MeV emitted at 7.3 km survive to 9.3 km without interaction. Immediately after creation, both leptons share the parent photon’s momentum, so the produced electron has a non-zero probability of being directed into the upper hemisphere. The angular distribution of leptons from  $\gamma \rightarrow e^+e^-$  pair production follows the classical Bethe–Heitler formulation (Bethe & Heitler, 1934), which predicts a strongly forward-peaked emission with characteristic angle:

$$\theta_0 \simeq \frac{1}{\gamma_e} \approx \frac{m_e c^2}{E_e}, \quad (8)$$

so the distribution is strongly forward-peaked along the incident  $\gamma$  direction. A simple conservative estimate of the backward-hemisphere tail can be obtained by approximating the angular distribution with a narrow Gaussian of width  $\theta_0$ . This gives

$$f_{\uparrow}(e | E_e) \approx e^{-\frac{(\pi/2)^2}{2\theta_0^2}} = e^{-\frac{\pi^2}{8}\gamma_e^2}, \quad (9)$$

which is a strict upper bound, since real BH kernels decrease even more steeply at large angles.

We combine the spectral weighting and backward-hemisphere acceptance into a single small factor  $f_{\uparrow\downarrow}$ , representing the solid-angle-weighted probability for a lepton to emerge opposite to the photon direction. For pair production, the electron typically carries a fraction  $x$  of the available energy  $(E_\gamma - 2m_e c^2)$ , with a mild preference for  $x \approx \frac{1}{2}$  (since  $d\sigma/dx \propto x^2 + (1-x)^2$ ). Weighting this by the  $E^{-2}$  photon spectrum and restricting initial photon-emission within  $\pm 45^\circ$ , the effective up-down acceptance does not exceed

Weighting these by the  $E^{-2}$  photon spectrum, and limiting gamma ray emitting angles by  $\pm 45$  degrees, a up-down directed coefficient  $f_{\uparrow\downarrow}$  will be  $\approx 10^{-5}$ , in agreement with angular distributions from Haug (1975).

Using an optimistic pair-production probability of  $P_{\text{pair}}(i) \sim 10^{-2}$  per 200 m slab (NIST XCOM database, Berger et al., 2010, Motz et al., 1969), a gamma-ray attenuation factor  $T=0.15$ , and 10 slabs in 2-km AEF, we obtain:

$$P(E_z, 9.3) = 10 \times P_{\text{pair}} \times f_{\uparrow\downarrow} e \times T = 1.5 \times 10^{-7} \quad (10)$$

Here, we assume that each of the ten 200-m slabs contributes roughly the same yield. Therefore, the total contribution across the 2-km gap is obtained by multiplying the yield of a single slab by 10. For a rough estimate of the gamma-ray output, we also adopt an optimistic RREA multiplication factor of  $\sim 10$  for both positron- and electron-driven avalanches. This simplification intentionally ignores the fact that the upward-moving electron RREA would restart in every slab, which would significantly decrease the effective multiplication. With these optimistic assumptions, the final expression becomes:

$$N_{\gamma}^{\uparrow}(9.3 \text{ km, from } e^+ \text{ and } e^- \text{ RREA}) = 2 \times \{M_{e^{\uparrow\downarrow}}^{\downarrow}(i, E_z, \gamma > 1.022 \text{ MeV}) \times P(E_z, 9.3)\} = 7.5 \times 10^{-4} \quad (11)$$

According to Eq. 2, each surviving upgoing gamma ray can again generate a downgoing positron with probabilities  $P_{\text{pair}} = 0.01$ , and downward emission  $f_{\text{down}} = 0.00001$ . Thus total expected number of recycling positrons will be

$$N_{e^+}^{\downarrow}(\text{recycling}) = N_{\gamma}^{\uparrow}(9.3 \text{ km, from } e^+ \text{ and } e^- \text{ RREA}) \times P_{\text{pair}}(9.3) \times f_{\downarrow e^+} \approx 10^{-10} \quad (12)$$

It is a total feedback return probability per cycle, meaning that infinite feedback is impossible. During CORSIKA simulations for the upper dipole at altitudes of 7.3-9.3 km, we consider all physical scenarios for upgoing seeds in the infinite relativistic feedback discharge model (RFD) proposed by Joe Dwyer (2003, 2025). Our approach provides a quantitative framework for interpreting experimental TGE spectra, modeling particle transport within AEF, and linking lepton interactions to the obtained simulations.

A key difference between the original RFD formulation and our approach lies in how the return probability for feedback particles is treated. In the RFD model, the feedback factor is defined as the product of the avalanche multiplication and an effective return efficiency, but the full probability chain leading to a downward-directed positron is not explicitly evaluated. In reality, a 1.022 MeV gamma ray reaching 9.3 km must (1) survive propagation over several hundred meters of atmosphere, and (2) undergo pair production with the positron emitted downward into the high-field region. Because pair production at MeV energies is strongly forward-peaked, the probability of downward emission is extremely small ( $f_{\text{down}} < 10^{-5}$ ). When combined with the pair-production probability per slab ( $P_{\text{pair}} \sim 10^{-2}$ ), the total recycling probability becomes  $\Gamma \approx 10^{-10}$ , as shown in Eq. (12). Even with avalanche gains ( $M \sim 10^4$ ), the resulting feedback coefficient remains negligible. Also, we didn't observe any signs of cycling in the loop in multiple CORSIKA simulations. The negligible probability of RFG strongly dismisses the possibility of infinite feedback, contradicting Dwyer's claim. It aligns with other RFD simulations by Stadnichuk et al. (2017) and Zelenyi et al. (2022), and Aragats' measurements (Chilingarian, 2017b; Chilingarian et al., 2024a) show a random avalanche particle arrival, confirming the absence of continuous particle flux expected for the RFD model.

Therefore, when directional and survival constraints are included, self-sustaining RFD is not achievable under realistic particle interaction conditions.

To estimate gamma-ray flux above 50 keV (the parameters used above are related to gamma-ray energies  $> 1.022$  MeV capable of pair-production) directed into open space, we will use different interaction parameters. We use the same probability of pair production in the 200 m slabs  $P_{\text{pair}} = 10^{-2}$ , but revised backscattering probability  $f_{50} = 0.2$  (related to backscattered Compton gamma rays), and 50 keV gamma-ray attenuation coefficient  $T_{50} = 0.06$  (reduced due to fast decline of low-energy gamma ray flux). With these parameters, Eqs. 10 and 11 yield a factor of  $P(\text{Ez}, 9.3\text{km}) \approx 2.4 \times 10^{-2}$ . Therefore, the likelihood of detecting 50 keV gamma rays traveling into open space, as per Eq. 11, is 24 per seed ambient positron. This is roughly 60 times higher than the CORSIKA estimate of 0.375. Assuming the flux of CR positrons at 9.3 km is about  $10^3$  per second per square meter, the total flux of gamma rays directed into open space would be  $10^4 \text{ m}^{-2} \text{ sec}^{-1}$ . We can add that we intentionally use optimistically biased estimates of all interaction parameters; therefore, this large discrepancy is not contradictory.

We propose an alternative seed mechanism that provides an external source of MeV gamma-ray seeds for the upper dipole, called a dual-stage model (DSM). The upward gamma-ray flux resulting from backscattered RREA gamma rays in the electron avalanche in the lower dipole (0.45 per seed electron, see the last row of 32) can produce electrons, which initiate RREA in the upper dipole. In Figure 10, we show a simulation of RREA development in the upper dipole, with a gamma-ray seed entering the lower boundary at 7.3 km. Born electrons travel in the same direction as gamma rays, so there is no penalty for backscattering, allowing a sizeable

multiplication of RREA particles. Assuming an ambient electron flux of  $1000 \text{ m}^{-2} \text{ sec}^{-1}$  and an RREA multiplication of 50 keV gamma-ray flux of 4000 (from Fig. 10), we estimate the flux of 50 keV gamma rays escaping from the upper dipole to be  $1.8 \times 10^6 \text{ m}^{-2} \text{ sec}^{-1}$ .

In contrast, the expected gamma ray flux from the inner seeds (ambient positron flux) is  $\approx 2 \times 10^3 \text{ m}^{-2} \text{ sec}^{-1}$ , which is 100 times more than from internal seeds in the upper dipole.

In 32, we present all quantitative estimates of upward gamma-ray flux. In Table 3, we summarize all the results on the upper dipole particle fluxes calculated and simulated in this section.

**Table 3. Summary of quantitative results on the considered mechanisms of the gamma-ray flux from the upper dipole**

Mechanism	Estimated Flux ( $\text{m}^{-2} \text{ s}^{-1}$ )	Notes
Ambient positron and electron flux in upper and lower dipoles	$1 \times 10^3$	Approximate estimate from EXPACS (Sato, 2016)
CORSIKA yield of $> 1$ MeV gamma-ray from lower dipole	0.45	Per seed electron
CORSIKA yield for 1 MeV gamma-ray in the upper dipole	4000	Electron avalanche in the upper dipole
CORSIKA yield for 50 keV gamma-ray to open space from DSM	$1.8 \times 10^6$	DSM flux: $1000 \times 0.45 \times 4000$
Theoretical estimate for 50 keV gamma-ray yield per inner ambient seed	24	Per seed positron
Corsika yield for 50 keV gamma-ray per inner ambient seed	0.375	We take an compromised estimate between CORSIKA and theoretical $\approx 1$
CORSIKA yield for 50 keV gamma-ray to open space from inner seed	$2 \times 10^3$	With a compromised estimate of per seed yield between CORSIKA and theoretical $\approx 2$
RFD infinite-feedback	$\approx 10^{-10}$	Recycling probability negligible; infinite feedback impossible

The DSM flux can be compared with measurements made by the ALOFT mission. However, the spectrometer onboard ALOFT has a detection threshold of about 300 keV (Ostgaard et al., 2024). Nonetheless, DSM estimates in the 50 keV–MeV range for 10 km fall within the BGO sensitivity band (Marisaldi et al., 2024) if the 10 km flux is transported to 20 km. This is possible because we position the tripole at 5.3–9.3 km, consistent with the Aragats location, and during tropical storms, the storm height can be much higher. Also, we reduce the DSM flux to the ALOFT spectrometer's threshold to approximately  $(1.1\text{--}1.3) \times 10^6 \text{ m}^{-2} \text{ s}^{-1}$ . The corrected value

aligns with the bright gamma-ray glows observed by ALOFT and falls between the lower and upper limits of ALOFT gamma fluxes, see Table 4.

**Table 4. The comparison of DSM flux estimates and registered ALOFT fluxes**

Source / Event	Flux at 10 km ( $\geq 300$ keV) ( $\text{m}^{-2} \text{s}^{-1}$ )	BGO Count Rate ( $\geq 300$ keV) 20 km	iSTORM Count Rate ( $\geq 300$ keV) 20 km
DSM Upper-Dipole (simulation, 10 km)	$1.1\text{--}1.3 \times 10^6$		
ALOFT (low)		$\approx 2.3 \times 10^2$	$\approx 8.1 \times 10^1$
ALOFT (high)		$\approx 7.8 \times 10^5$	$\approx 2.7 \times 10^5$

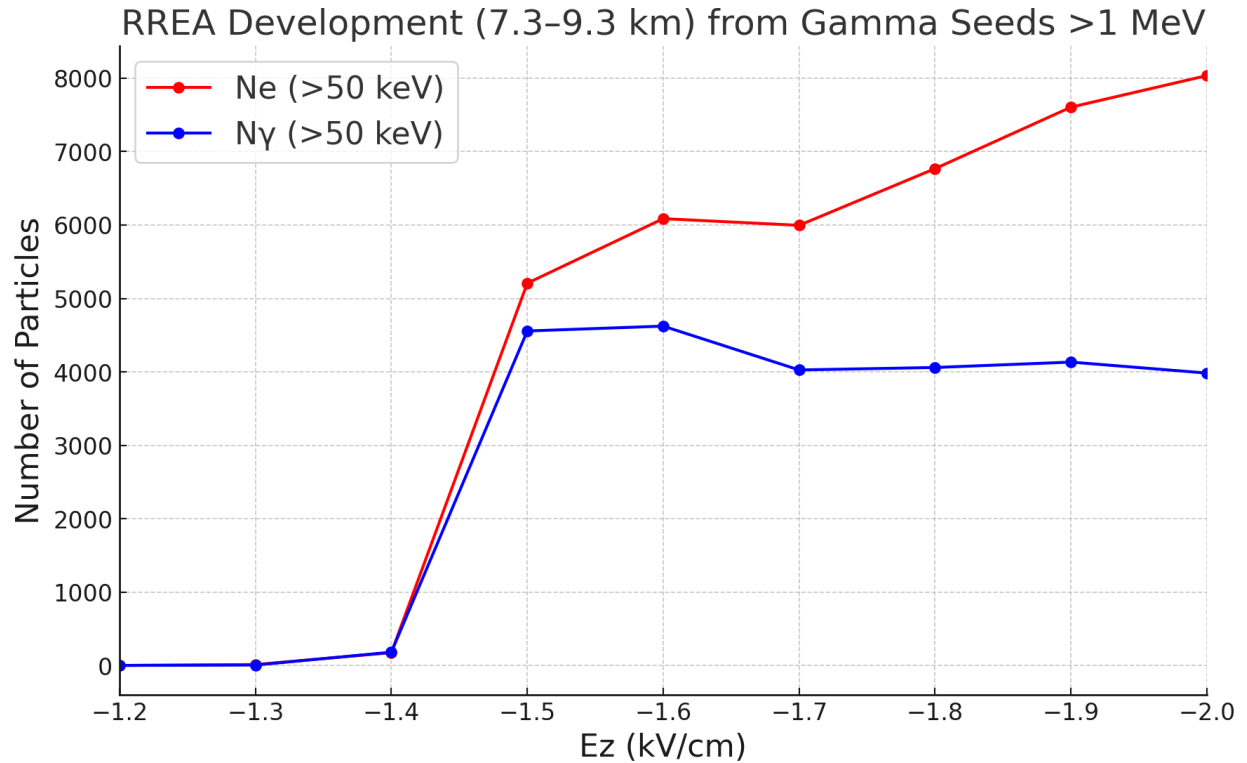


*Figure 10. Multiplication of RREA particles per seed gamma ray with energy larger than 1 MeV in the upper dipole.*

Another interesting result shown in Fig. 10 is that, as the AEF increases, the gamma rays produced in electron RREA reach a peak at 1.5 kV/cm and then level off, even decreasing with further increases of the electric field. Rare air reduces high-energy electron interactions, resulting in fewer gamma rays in RREA. The effect of rare air, reduces optimal AEF, when number of

gamma rays in the RREA is maximum, and overall the optimal AEF with altitude is reducing, as seen in Fig. 11.

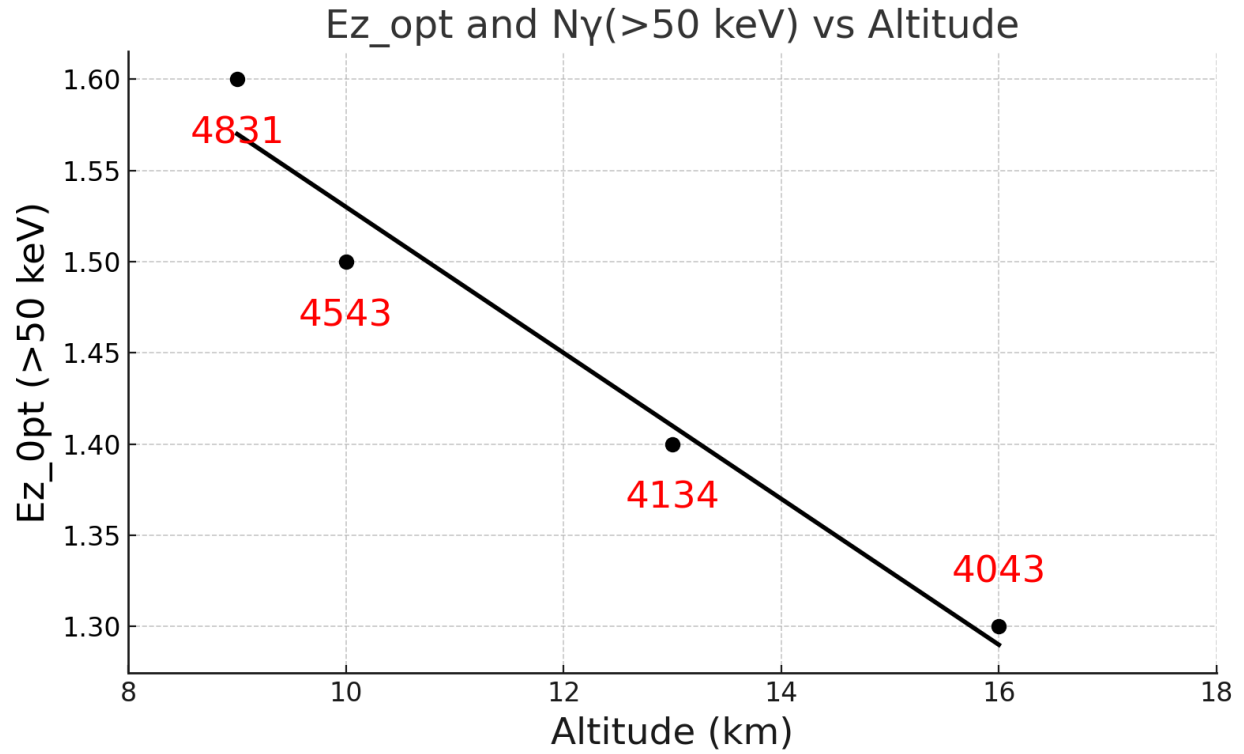


Figure 11. Latitude dependence of optimal AEF (for maximum gamma rays in the avalanche). My red numbers were denoted gamma ray maximums among the tested 1-2 kV/cm electric fields.

Therefore, the multiplication of gamma rays at high altitudes is limited, and there is no need to use unnecessarily high AEF values in RREA simulations.

## 7. Model of the DTGF origination

Wada et al. (2025) propose a DTGF model based on converging positive and negative leaders, which was observed on January 30, 2023, in Kanazawa, Japan. A 31- $\mu$ s gamma-ray burst detected by scintillators was accompanied by lightning leader detection, resulting in cloud-to-ground lightning (-CG). A downward negative leader initiated at an altitude of 2 to 3 km extends toward the ground. The upward positive leader propagated from the tower, see Fig. 12). The first gamma rays of the downward TGF started 31  $\mu$ s before the return stroke and reached saturation level 17  $\mu$ s before RS. This suggests that the TGF occurred when the upward and downward leaders were approaching and just before they collided.

The authors assume that a strong electric field in the narrow gap between approaching leaders initiates RREA. However, they overlook fundamental constraints imposed by avalanche physics on the spatial extent of the electric field responsible for RREA. The observed DTGF duration,  $\Delta t \approx 31 \mu$ s, along with the stepped leader approach speed ( $v \approx 1.8 \times 10^6$  m/s, Wada, 2025), suggests that electron acceleration continues when the gap distance is less than:  $\Delta h = v \cdot \Delta t \approx 1.8 \cdot 10^6$  m/s

$\cdot 31 \cdot 10^{-6} \text{ s} \approx 56 \text{ m}$ .

The characteristic avalanche (e-folding) length for RREA at near-ground pressure is approximately 70 meters (Celestin & Pasko, 2011; Dwyer et al., 2012); also see discussion at the beginning of section 5. Efficient avalanche multiplication, necessary for observable DTGF production, requires several e-folding lengths to be available before the rapidly closing gap between the two leaders. This implies that if the acceleration region were confined to the leader–leader gap, RREA and significant gamma-ray emission would not be possible.

The DTGF terminates when the potential difference is neutralized by leader reconnection. In this model, the upward positive leader does not initiate the DTGF; instead, it terminates it by neutralizing the potential difference between the negative leader and Earth, explaining the abrupt cessation of the gamma-ray burst. The acceleration process is thus sustained in the full vertical leader–ground gap, rather than in the narrow region between the approaching leader tips (see Figure 9).

Multiyear DTGF observations in Uchinada, Japan, are also linked to negative cloud-to-ground lightning, demonstrating that gamma-ray fluxes span a vast area of at least 100 km<sup>2</sup> around the lightning flash (see Fig. 1 of Ortberg et al., 2024). This raises a fundamental question: how can a small negative leader tip, only a few cm<sup>2</sup> in size, influence atmospheric electric fields over 5 kilometers to initiate RREA across extensive cloud volumes (see Fig.12)?

In contrast, the downward propagation of a negative leader in a pre-critical dipole field between the main negative (MN) layer and image charges near the ground can induce a non-local reorganization of the AEF. Thus, the negative leader acts not as a direct accelerator but as a trigger for large-scale field transformation, displacing equipotential surfaces and enhancing preexisting subcritical fields over vast volumes. As the negative leader descends, it effectively 'pulls down' the potential of the MN layer, compressing the equipotential surfaces below it. This deformation increases the local electric field between the MN layer and the ground, transforming previously subcritical regions into zones that extend 800 m vertically and 10 km horizontally, capable of initiating RREA. This mechanism, demonstrated by the detection of hundreds of TGEs worldwide (Chilingarian et al., 2025), allows extensive areas, spanning many square kilometers, to experience a deepening of negative AEF from modest to supercritical levels. Thus, the DTGFs observed in Uchinada receive a natural explanation within the large-scale extension of AEF in the lower dipole, rather than assuming an enigmatic source of  $10^{19}$  electrons above 1.5 km from the surface.

Recent observations by the Telescope Array Surface Detector (TASD) also linked DTGFs to downward negative leaders traveling at a velocity greater than  $3 \times 10^6 \text{ m/s}$ , which result in -CG-lightning flashes (Kieu et al., 2025). They didn't report upward lightning leaders but confirmed the relationship between TGF production and fast downward negative leaders, as suggested by Wu et al. (2021).

TGEs are initiated in the strong AEFs, surpassing the RREA threshold values, and their development—sometimes lasting for a few tens of minutes—was not accompanied by lightning activity. However, the inverted intracloud (-IC), -CG, or hybrid flashes (beginning as -IC and then turning into -CG) often ended the TGEs. Recent analysis of 163 TGEs terminated by lightning flashes at Aragats demonstrates that the share of -CGs, -ICs, and hybrid flashes is

significantly higher, at 92.7%, compared to the share of normal polarity ICs, which is only 11.3% (Chilingarian, Rakov, and Khanikyannc, 2024).

Thus, the proposed DTGF model aligns with DTGF observations at Uchinada, Utah, and recent gamma glows (Marisaldi et al. 2024; Ostgaard et al., 2024), and multi-year observations of thunderstorm ground enhancements (TGEs) by the SEVAN network. (Chilingarian et al., 2010; 2011). These observations reveal that high-energy particle bursts can affect regions covering many square kilometers before lightning occurs.

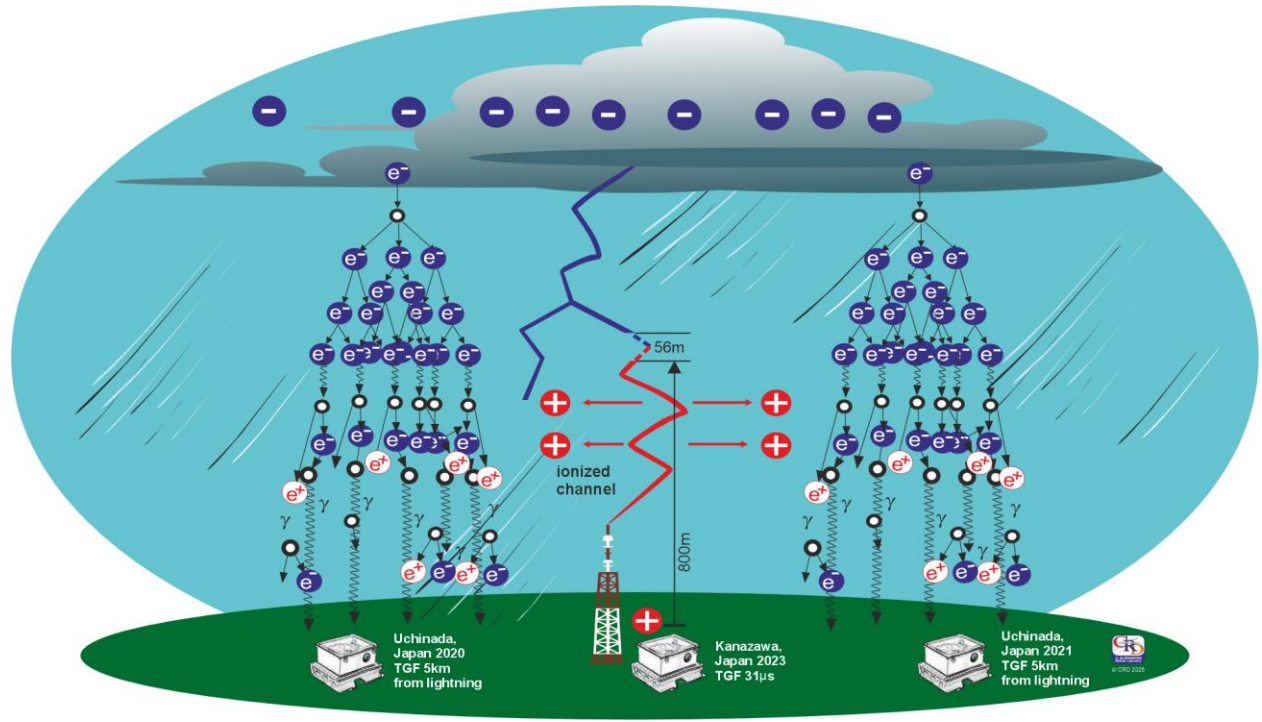


**Figure 12. Revised DTGF model. Approaching lightning leaders (center) induce non-local reorganization of the atmospheric electric field (AEF), transforming previously subcritical regions into RREA-capable zones. RREA regions are shown at distances of ~5 km from the lightning channel, consistent with observations in Uchinada (2020–2021).**

**Blue – downward negative leader; red – upward positive leader.**

## 8. Discussion and Conclusions

Relativistic runaway electron avalanches cause thunderstorm ground enhancements, gamma-ray glows, and both upward and downward terrestrial gamma flashes. Recognizing the common origin for microsecond TGFs, minute-long gamma glows, and TGEs indicates progress toward accepting RREA and EAS as universal physical processes that produce increased particle fluxes in both the lower and upper atmosphere. For this ambitious program, the most challenging task is identifying the seed sources for the upward gamma rays from the upper dipole.

Several mechanisms have been proposed for the origin of seed electrons. The photoelectric model (Pasko et al., 2025) suggests that X-ray-driven photoionization produced within the relativistic feedback framework photo-ionize air molecules, liberating electrons even below the runaway threshold. While effective in explaining lightning initiation at leader tips, this model operates on very short timescales ( $\mu\text{s}$ – $\text{ms}$ ) and does not directly account for sustained, seconds-minutes-long MeV gamma glows observed far from leader channels.

The cold-runaway model (Celestin & Pasko, 2011) mainly examines runaway electron production at lightning-leader tips, where very intense, localized electric fields can accelerate low-energy (“cold”) electrons to relativistic energies. Their model aims to explain the high initial electron fluxes that seed leader-associated TGFs and naturally functions on microsecond timescales within tens of meters around the leader channel.

Dwyer’s relativistic feedback model (RFD, Dwyer, 2003) is a single-region, closed-loop mechanism (infinite feedback) where the ambient population of cosmic rays generates backward-moving positrons that re-enter the same high-field layer, thereby sustaining the avalanche.

In contrast, the proposed double-stage model involves two regions and a feedforward process: the lower dipole supplies MeV photon seeds to the upper dipole, which are converted into upward electrons that trigger RREA in the upper dipole. This setup naturally accommodates kilometer-scale field gaps, large horizontal footprints, and lightning-silent, minutes-long glows observed by aircraft and balloons. Relativistic feedback may still operate within each dipole and slightly modify the local multiplication, but it will not close the loop across the gap and does not alone explain the altitude, duration, and areal extent of the upward glows. The altitude range, intensity, duration, and frequent radio silence reported in the ALOFT campaign align with the predicted upward transport and amplification in the upper dipole described by the dual-stage model.

Observed DTGFs cover large areas and last tens of microseconds, with duration, intensity, and spatial scales that are hard to reconcile with RREA confined to a narrow leader–leader gap. The e-folding length near ground pressure suggests that several e-foldings are needed. However, a 56 m length that closes in 31  $\mu\text{s}$  cannot provide enough path for avalanche development and strong gamma multiplication. Instead, in our view, a descending negative leader in a pre-critical lower-dipole field reorganizes the AEF non-locally, deepening subcritical regions into supercritical ones over hundreds of meters vertically and kilometers horizontally. This process enables RREA over a wide footprint. Reconnection then quickly quenches the potential drop, explaining the sudden end of DTGFs. This non-local field reorganization naturally links DTGFs with TGEs and glows, all of which are manifestations of RREA in different geometries.

Nevertheless, we fully acknowledge that *special* meteorological conditions, such as Japanese winter thunderstorms, may support a different class of gamma-ray events. Although downward

TGFs associated with compact lightning strokes have recently been reported over Japan (Wu et al., 2025), long-term measurements at Aragats and the combined optical-particle observations from ASIM and ALOFT show that TGEs and gamma-ray glows are not triggered by lightning; lightning activity typically suppresses or terminates them. Yet, no confirmed mechanism exists by which lightning processes could provide the required upward-directed MeV seed electrons for RREA.

Various physical processes drive atmospheric particle fluxes, making it essential to accurately identify each one. Since TGE research began at Aragats in 2010, nearly 1,000 TGEs have been recorded on mountaintops across Eastern Europe, Japan, Russia, Germany, and Armenia (Chilingarian et al., 2025). Early observations of gamma-ray bursts are already reviewed and discussed comprehensively in Chilingarian (2024); here, we focus on the particle-flux characteristics of gamma glows in lower and upper dipoles as revealed by recent ALOFT and ASIM measurements. Recent observations have been made at Mt. Hermon in Israel (Mauda et al., 2025) and in Finland (Kärkkäinen et al., 2024). Measurements of TGE electrons and gamma rays confirmed RREA as a viable electron accelerator covering many square kilometers on Earth's surface. Along with simulations, these findings have provided a detailed understanding of RREA development and cloud charge structures in the lower atmosphere. According to DSM, the seed electrons for TGE are free electrons from EASs, while gamma glow seeds originate from RREA in the lower atmosphere in the form of reverting gamma rays. The atmospheric electric field in the upper and lower dipoles, ranging from 1.4 to 2.1 kV/cm, is sufficient to trigger RREAs at altitudes of 3-15 km. Enhanced electric fields and seed particles moving both downward and upward can explain the energy spectra of electrons and gamma rays in measured TGEs, as well as the intensity of gamma glows. During DTGF, the rearrangement of the electric field through lightning leader interactions increases pre-critical AEF to levels sufficient for the runaway process.

Gaining a deeper understanding of different charge structures and the hierarchy of particle acceleration mechanisms will clarify the high-energy phenomena observed in thunderstorms and their implications for atmospheric science.

## Reference

Alexeenko V.V, Khaerdin.ov N.S, Lidvansky A.S, et al. (2002). Transient variations of secondary cosmic rays due to the atmospheric electric field and evidence for pre-lightning particle acceleration. *Phys Lett A* 301:299 306.

Ambrozová I., Kákona M., Dvorák R., et al. (2023) Latitudinal effect on the position of Regener–Pfozter maximum investigated by balloon flight HEMERA 2019 in Sweden and balloon flights FIK in Czechia, *Radiation Protection Dosimetry* 199(15–16), 2041.  
[doi.org/10.1093/rpd/ncac299](https://doi.org/10.1093/rpd/ncac299)

Auger P., Ehrenfest P., Maze, R., et al.: 1939, Extensive Cosmic-Ray Showers, *Reviews of Modern Physics*, 11, 3–4, 288–291. doi.org/10.1103/RevModPhys.11.288

Babich, L. P., Donskoy, E. N., Kutsyk, I. M., & Kudryavtsev, A. Y. (2001). Comparison of relativistic runaway electron avalanche rates obtained from Monte Carlo simulations and kinetic equation solution. *IEEE Transactions on Plasma Science*, 29(3), 430-438.

Babich, L.P. 2007. Reanalysis of experimental results on runaway breakdown. *Journal of Geophysical Research*, 112, D09301.

Berger, M.J. et al. 2010. XCOM: Photon Cross Section Database. National Institute of Standards and Technology PML, Radiation Physics Division.  
<https://dx.doi.org/10.18434/T48G6X>.

Bethe, H. & Heitler, W. (1934) ‘On the stopping of fast particles and on the creation of positive electrons’, *Proceedings of the Royal Society A*, 146(856), pp. 83–112.  
<https://doi.org/10.1098/rspa.1934.0140>. [Royal Society Publishing+1](#)

Bjørge-Engeland, I., Østgaard, N., Sarria, D., et al. (2024). Evidence of a New population of weak Terrestrial Gamma-Ray flashes observed from aircraft Altitude, *Geophysical Research Letters*, 51, e2024GL110395. doi.org/10.1029/2024GL110395

S. Buitink, H. Falcke, et al. Monte Carlo simulations of air showers in atmospheric AEFs, *Astropart. Phys.* 33 1, 2010.

Celestin, S., & Pasko, V. P. (2011). Energy and fluxes of thermal runaway electrons produced by the exponential growth of streamers during the stepping of lightning leaders and in transient luminous events. *Journal of Geophysical Research (Space Physics)*, 116, 3315. doi: 10.1029/2010JA016260

Chilingarian A., A. Daryan, K. Arakelyan, et al. (2010) Ground-based observations of Thunderstorm-correlated fluxes of high-energy electrons, gamma rays, and neutrons, *Phys. Rev. D* 82, 043009. doi: 10.1103/PhysRevD.82.043009

Chilingarian A, Hovsepyan G., and Hovhannisyan A. (2011) Particle bursts from thunderclouds: Natural particle accelerators above our heads, *Phys. Rev. D* 83, 062001. doi.org/10.1103/PhysRevD.83.062001

Chilingarian A., Bostanjyan N., Vanyan L., (2012) Neutron bursts associated with thunderstorms, *Phys. Rev. D* 85, 085017.

Chilingarian A., Hovsepyan G., Khanikyanc Y., Reymers A., and Soghomonyan S. (2015) Lightning origination and thunderstorm ground enhancements terminated by the lightning flash, *Europhysics Letters*, 110, 49001. Doi: 10.1209/0295-5075/110/49001

Chilingarian A., Chilingaryan S., Karapetyan T., et al. (2017a) On the initiation of lightning in thunderclouds, *Scientific Reports* 7, Article number: 1371, doi:10.1038/s41598-017-01288-0.

Chilingarian A., Hovsepyan G., Mailyan B., 2017b. In situ measurements of the Runaway Breakdown (RB) on Aragats mountain, *Nuclear Inst. and Methods in Physics Research*, A 874,19–27.

Chilingarian A., Babayan V., Karapetyan T., et al. (2018) The SEVAN Worldwide network of particle detectors: 10 years of operation, *Advances in Space Research* 61, 2680.

Chilingarian, Ashot; Hovsepyan, Gagik (2021), “Dataset for 16 parameters of ten thunderstorm ground enhancements (TGEs) allowing recovery of electron energy spectra and estimation of the structure of the electric field above Earth’s surface”, Mendeley Data, V3, doi: 10.17632/tvbn6wdf85.3 <https://data.mendeley.com/datasets/tvbn6wdf85/3>

Chilingarian, G. Hovsepyan, E. Svechnikova, and M. Zazyan 2021b. Electrical structure of the thundercloud and operation of the electron accelerator inside it, *Astroparticle Physics* 132(2021) 102615 <https://doi.org/10.1016/j.astropartphys>

Chilingarian A., Karapetyan T., Zazyan M. et al. 2021c. Maximum strength of the atmospheric electric field, *PRD*, 2021, 103, 04302.

Chilingarian A., Hovsepyan G., Karapetyan G., and Zazyan M. (2021b) Stopping muon effect and estimation of intracloud electric field, *Astroparticle Physics* 124 102505.

Chilingarian A., Hovsepyan G. (2022), The synergy of the cosmic ray and high energy atmospheric physics: Particle bursts observed by arrays of particle detectors, *New Astronomy*, 97, 101871.

Chilingarian A., Hovsepyan G., Aslanyan D., et al. 2023. Thunderstorm ground enhancements observed on Aragats Mountain in Armenia during the winter, *EPL* 143, 59002, supplemented materials. doi.org/10.1209/0295-5075/acf340

Chilingarian A.(2024) Extensive air showers and atmospheric electric fields. Synergy of space and atmospheric particle accelerators, *Advances in Space Research* 74, 4388. doi.org/10.1016/j.asr.2024.03.013

Chilingarian A., Khanikyants Y., Rakov V. (2024) Corrigendum to Termination of thunderstorm-related bursts of energetic radiation and particles by inverted intracloud and hybrid lightning discharges, *Atmospheric Research*, 233 (2020), 104713-104720. doi.org/10.1016/j.atmosres.2024.107403

Chilingarian A., Sargsyan B., Karapetyan T., et al. (2024a) Extreme thunderstorm ground enhancements registered on Aragats in 2023, *Physical Review D* 110, 063043a

Chilingarian A., Sargsyan B. (2024b) Atmospheric positron flux modulation during thunderstorms, *Physical Review D* 109, 062003. doi:10.1103/PhysRevD.109.062003

Chilingarian A., Karapetyan T., Sargsyan B., Khanikyanc Y., and Chilingaryan S. (2024c) Measurements of Particle Fluxes, Electric Fields, and Lightning Occurrences at Aragats Space-Environmental Center (ASEC), *Pure and Applied Geophysics* 181, 1963. <https://doi.org/10.1007/s00024-024-03481-5>

Chilingarian A., Pokhsranyan D., Zagumennov F., Zazyan M. (2024d) Space-temporal structure of the thunderstorm ground enhancements (TGEs), *Physics Open* 18, 100202. doi.org/10.1016/j.physo.2023.100202

Chilingarian A., Karapetyan T., Sargsyan B., Knapp J., Walter M., Rehm T.(2024e) Energy spectra of the first TGE observed on Zugspitze by the SEVAN light detector compared with the energetic TGE observed on Aragats, *Astroparticle Physics* 156, 02924. doi: 10.1016/j.astropartphys.2024.102924

Chilingarian, A., Williams, E., Hovsepyan, G., & Mkrtchyan, H. (2025). Why Schonland failed in his search for runaway electrons from thunderstorms. *Journal of Geophysical Research: Atmospheres*, 130, e2024JD042350. doi.org/10.1029/ 2024JD042350

Chum, R. Langer, J. Baše, M. Kollárik, I. Strhářský, G. Diendorfer, J. Rusz (2020) Significant enhancements of secondary cosmic rays and electric field at high mountain peak during thunderstorms, *Earth Planets Space* 72, 28. doi.org/10.1186/s40623-020-01155-9

Dwyer J.R. (2003) A fundamental limit on electric fields in air, *Geophys. Res. Lett.* 30, 2055. doi.org/10.1029/2003GL017781

Dwyer, J. R., and L. P. Babich (2011), Low-energy electron production by relativistic runaway electron avalanches in air, *J. Geophys. Res.*, 116, A09301, doi:10.1029/2011JA016494.

Dwyer J.R., Smith D.M., Cummer S.A. (2012) High-Energy Atmospheric Physics: Terrestrial Gamma-Ray Flashes and Related Phenomena, *Space Sci Rev* 173, 133.  
DOI 10.1007/s11214-012-9894-0

Dwyer J.R., Rassoul H.K. (2024) High energetic radiation from thunderstorms and lightning, in *Lightning Electromagnetics*, IET series Volume 1, 365.

Dwyer, J.R.(2025). Energetic particles are produced by thunderstorm electric fields.  
*Journal of Geophysical Research: Atmospheres*,130,e2024JD042193.  
<https://doi.org/10.1029/2024JD042193>

Feynman R., Leighton R.B., Sands M., 1963.The Feynman Lectures on Physics Vol. II Ch. 9- Electricity in the Atmosphere, edited by M.A. Gottlieb and R. Pfeiffer, California Institute of Technology.

Fishman G. J., Bhat P.N., Mallozzi R., et al. (1994) Discovery of Intense Gamma-Ray Flashes of Atmospheric Origin, *Science*, 264, 1313. doi/science.264.5163.1313

Fuglestad A. N., Multi Pulse Terrestrial Gamma-ray Flashes and optical pulses of lightning observed by ASIM, Master Thesis in Space Physics, University of Bergen <https://bora.uib.no/bora-xmloi/bitstream/handle/11250/3073302/Multi-Pulse-Terrestrial-Gamma-ray-Flashes-and-optical-pulses-of-lightning-observed-by-ASIM-print-version.pdf?sequence=3&isAllowed=y>

Engel, R., Heck, D. and Pierog, T. 2019. CORSIKA 8—A modern framework for particle-cascade simulations. *Computing and Software for Big Science*, 3, 2.DOI: [10.22323/1.484.0045](https://doi.org/10.22323/1.484.0045)

Heck D., Knapp J., Capdevielle J. N., Schatz G., and Thouw T., Report No. FZKA 6019, 1998, Forschungszentrum, Karlsruhe, <https://www.ikp.kit.edu/corsika/70.php>.

Heitler, W. (1954) *The Quantum Theory of Radiation*. 3rd edn. Oxford: Clarendon Press.

Gourbin, P., Celestin, S. (2024). On the self-quenching of relativistic runaway, electron avalanches producing terrestrial gamma-ray flashes: *Geophysical Research Letters*, 51(10), e2023GL107488.

Gurevich, G., Milikh, R., Roussel-Dupre (1992) Runaway electron mechanism of air breakdown and preconditioning during a thunderstorm, *Physics Letters A* 165 (5), 463.

Haug, E. 1975. Bremsstrahlung and pair production in the field of free electrons. *Z. Naturforsch. A*, 30, pp.1099–1113.

Helmerich, C., McKinney, T., Cavanaugh, E., & Dangelo, S. (2024) TGFs, gamma-Ray glows, and direct lightning strike radiation is observed during a single flight of a balloon-borne gamma-ray spectrometer, *Earth and Space Science*, 11, e2023EA003317. doi.org/10.1029/2023EA003317

Kelley N.A., Smith D.M., Dwyer J.R., et al. (2015) Relativistic electron avalanches as a thunderstorm discharge competing with lightning, *Nature Communications*, 6 (7845). doi.org/10.1038/ncomms8845

Kieu, N., Abbasi, R. U., Saba, M. M. F., et al. (2025). Time-resolved leader spectra of downward Terrestrial Gamma-ray Flashes observed at the Telescope Array Surface Detector. *Journal of Geophysical Research: Atmospheres*, 130, e2025JD043812. <https://doi.org/10.1029/2025JD043812>

Klein, O. and Nishina, Y. (1929) ‘Über die Streuung von Strahlung durch freie Elektronen nach der neuen relativistischen Quantendynamik von Dirac’, *Zeitschrift für Physik*, 52, pp. 853–868. doi: 10.1007/BF01366453

Kochkin P., Van Deursen P., Marisaldi M., et al. (2017) In-flight observation of gamma-ray glows by ILDAS. *JGR, Atmos* 122:12801–12811. doi: 10.1002/2017JD027405

Kuettner, J. (1950). The electrical and meteorological conditions inside thunderclouds. *J. Meteorol.*, 7, 322–332. doi.org/10.1175/1520-0469(1950)007<0322:TEAMCI>2.0.CO;2

Lang T.J., Østgaard N., Marisaldi M. et al., Hunting for Gamma Rays above Thunderstorms: The ALOFT Campaign, *Bulletin of the American Meteorological Society*. doi.org/10.1175/BAMS-D-24-0060.1

Leppänen, A-P., K. Peräjärvi<sup>1</sup>, J. Paatero, J. Joutsenvaara, A. Hannula, A. Hepoaho, P. Holm, J. Kärkkäinen (2024), Thunderstorm ground enhancements in Finland: observations using spectroscopic radiation detectors, *Acta Geophysica*, <https://doi.org/10.1007/s11600-024-01495-0>

Lindanger, A., Marisaldi, M., Sarria, D., Østgaard et al. (2021) Spectral analysis of individual terrestrial gamma-ray flashes detected by ASIM. *Journal of Geophysical Research: Atmospheres*, 126, e2021JD035347. doi.org/10.1029/2021JD035347

Marisaldi M., Østgaard N., Mezentsev A., et al. (2024). Highly dynamic gamma-ray emissions are common in tropical thunderclouds, *Nature* 634, 57.

MacGorman, D. R. and Rust, W. D., The Electrical Nature of Storms, Oxford University Press, New York, NY, 1998.

McCarthy, M., and Parks, G. (1985). Further observations of X-rays inside thunderstorms, *Geophysical Research Letters*, 12, 393. doi.org/10.1029/GL012i006p00393

Mailyan B.G., Briggs M. S., Cramer E. S., et al. (2016). The spectroscopy of individual terrestrial gamma-ray flashes: Constraining the source properties, *J. Geophys. Res. Space Physics*, 121, 11,346–11,363. doi.org/10.1002/2016JA022702

Mauda N., Yair. Y, Reuveni Y., Multi-parametric analysis of thunderstorm ground enhancements (TGE) and associated gamma-ray emissions on Mount Hermon, Israel, *Science of the Total Environment* 993 (2025) 179988. https://doi.org/10.1016/j.scitotenv.2025.179988

Motz, J.W., Olsen, H.A. & Koch, H.W. 1969. Pair production by photons. *Reviews of Modern Physics*, 41, pp.581–639.

Nag, A., Rakov, V. (2009) Some inferences on the role of lower positive charge region. in facilitating different types of lightning. *Geophys. Res. Lett.* 36, L05815.

Neubert, T., Østgaard, N., Reglero, V., Blanc, E., Chanrion, O., Oxborrow, C. A., et al. (2019) The ASIM mission on the International Space Station. *Space Science Reviews*, 215(2), 26. doi.org/10.1007/s11214-019-0592-z

Ortberg, J., Smith, D. M., Kamogawa et al. (2024). Two laterally distant TGFs from negative cloud-to-ground strokes in Uchinada, Japan. *Journal of Geophysical Research: Atmospheres*, 129, e2023JD039020. https://doi.org/10.1029/2023JD039020.

Ostgaard, N., Christian, H. J., Grove, J. E., Sarria, D., Mezentsev, A., Kochkin, P., et al. (2019) Gamma-ray glow observations at 20-km altitude. *Journal of Geophysical Research: Atmospheres*, 124, 7236–7254. doi.org/10.1029/2019JD030312.

Østgaard, N., Christian, H. J., Grove, J. E., Sarria, D., Mezentsev, A., Kochkin, P., et al. 2019. Gamma rayglow observations at 20-km altitude. *Journal of Geophysical Research: Atmospheres*, 124, 7236–7254.

Østgaard N., Marisaldi M., Mezentsev A., et al. 2024. Flickering gamma-ray flashes, the missing link between gamma glows and TGFs, *Nature* 634, 53.

Parks, G.K., Mauk, B.H., Spiger, R., Chin, J. (1981) X-ray enhancements detected during thunderstorm and lightning activities. *Geophys. Res. Lett.* 8, 1176–1179, doi.org/10.1029/GL008i011p01176.

Pallu, M., Celestin, S., Hazem, Y., Trompier, F., & Patton, G. (2023). XStorm: A new gamma ray spectrometer for detecting close proximity gamma ray glows and TGFs. *Journal of Geophysical Research: Atmospheres*, 128, e2023JD039180. <https://doi.org/10.1029/2023JD039180>

Pasko, V. P., Celestin, S., Bourdon, et al. (2025). Photoelectric effect in air explains lightning initiation and terrestrial gamma ray flashes. *Journal of Geophysical Research: Atmospheres*, 130, e2025JD043897. <https://doi.org/10.1029/2025JD043897>

Regener, E., and Pfozter, G. (1934). Intensity of cosmic ultra-radiation in the stratosphere with the tube counter. *Nature* 134, 325.

Roussel-Dupré R., Symbalisty E., Taranenko Y., Yukhimuk V. (1998) Simulations of high-altitude discharges initiated by runaway breakdown, *J. Atmos. Sol.-Terr. Phys.* 60, 917–940. doi.org/10.1016/S1364-6826(98)00028-5

Sato, T. Analytical model for estimating the zenith angle dependence of terrestrial cosmic ray fluxes. *PLoS ONE* **2016**, 11, e0160390.

Skeie, C. A., Østgaard, N., Mezentsev, et al. (2022). The temporal relationship between terrestrial gamma-ray flashes and associated optical pulses from lightning. *Journal of Geophysical Research: Atmospheres*, 127, e2022JD037128. doi.org/10.1029/2022JD037128

Spread: available online: <https://www.omnicalculator.com/physics/cloud-base> (accessed on 1 August 2025).

Sommer M., Czakoj T., Ambrožová<sup>1</sup>I., et al., Exploring the Potential of Aerial and Balloon–Based Observations in the Study of Terrestrial Gamma-Ray Flashes, preprint. doi.org/10.5194/egusphere-2024-2789

Stadnichuk, V., Babich, L.P. & Donskoy, E.N. 2017. Numerical simulation of relativistic runaway breakdown. *Physics of Plasmas*, 24, 033502.

Stolzenburg, M. et al. 2007. Electrical structure in thunderstorms. *Journal of Geophysical Research*, 112, D13201.

Symbalist, E. M. D., R. A. Roussel-Dupré, and V. A. Yukhimuk (1998), Finite volume solution of the relativistic Boltzmann equation for electron avalanche studies, *IEEE Trans. Plasma Sci.*, 26, 1575–1582.

Tsuchiya, H., Enoto, T., et al. (2012). Observation of thundercloud-related gamma rays and neutrons in Tibet. *Phys. Rev. D* 85, 092006.

Zhang, H., Lu, G., Liu, F., Xiong, S., Ahmad, M. R., Yi, Q., et al. (2021) On the Terrestrial Gamma-ray Flashes preceding narrow bipolar events. *Geophysical Research Letters*, 48, e2020GL092160. Doi. [org/10.1029/2020GL092160](https://doi.org/10.1029/2020GL092160)

Zelenyi, L.M., et al. 2022. Relativistic atmospheric feedback simulation. *Journal of Atmospheric and Solar–Terrestrial Physics*, 229, 105765

Ursi A., Virgili D., Campana R., et al. (2024). Detection of an Intense Positron Burst During a Summer Thunderstorm on Mt. Etna, AGU fall meeting AE01-04

Wada, Y., Enoto, T., Kubo, M., Nakazawa, K., Shinoda, T., Yonetoku, D., et al. (2021). Meteorological aspects of gamma-ray glows in winter thunderstorms. *Geophys. Res. Lett.*, 48(7). <https://doi.org/10.1029/2020gl091910>

Wada, Y., Morimoto T., Wu T., et al. (2025). Downward terrestrial gamma- ray flash associated with collision of lightning leaders, *Science Advances*, 11, eads6906.

Williams E., The tripole structure of thunderstorms, *JGR* 94 (1989), 13151.

Wu, T., Wang, D., Huang, H., & Takagi, N. (2021). The strongest negative lightning strokes in winter thunderstorms in Japan. *Geophysical Research Letters*, 48(21), e2021GL095525. <https://doi.org/10.1029/2021gl095525>

Wu, T., Smith, D. M., Wada, Y. et al. (2025). Energetic compact strokes as the major source of downward terrestrial gamma-ray flashes in winter thunderstorms. *Geophysical Research Letters*, 52, e2024GL113194. [doi.org/10.1029/2024GL113194](https://doi.org/10.1029/2024GL113194)

## **Notations:**

The following terminology pertains to the atmospheric fluxes of elementary particles produced during thunderstorms:

- Terrestrial gamma-ray flashes (TGFs) are short bursts of gamma radiation detected by orbiting gamma-ray observatories. They last for tens of microseconds, originate from

thunderstorms in equatorial regions, and are observed by the orbiting gamma-ray observatories positioned 400 to 700 kilometers above the source.

- TGEs (thunderstorm ground enhancements) refer to intense and prolonged particle fluxes observed on the Earth's surface, lasting from seconds up to several tens of minutes. These fluxes originate from the same RREA process; the accelerating electric fields are located just above the detectors (sometimes 25-100 m), allowing for a detailed study of the energy spectra of electrons and gamma rays, as well as the charge structures of thunderclouds.
- Gamma glows are bursts of gamma radiation from RREAs in the upper dipole detected high in the atmosphere by instruments carried on balloons or aircraft. These events can last from tens of seconds to several minutes and typically conclude with a lightning strike.
- The gamma-ray enhancements observed at the Earth's surface are sometimes also called gamma glows because thunderclouds, due to their high altitude, exclusively detect gamma rays and no other types of radiation particles (Wada et al., 2021).
- The lightning leaders can initiate downward TGFs by triggering a large-scale field transformation, displacing equipotential surfaces and enhancing preexisting subcritical electric fields over vast thunderstorm volumes.
- AEF – Atmospheric Electric field
- Dual-stage model (DSM) in which RREA development in the lower dipole generates upward-directed gamma rays that seed RREA in the upper dipole.
- Relativistic Feedback Discharge (RFD) cycling infinite loop model in the upper dipole